AN ESTIMATION OF RISK OF COLLES' FRACTURE USING MODEL-BASED INTERPRETATION OF BONE PROFILES

by

SAWASDICHAI ARAYA

A thesis submitted to
the University of Birmingham for the degree of
MASTER BY RESEARCH

Department of Electronic, Electrical and Computer Engineering

Faculty of Engineering

The University of Birmingham

Apirl 2010

ABSTRACT

In this thesis a technique to estimate the risk of Colles' fracture using ordinary radiographs, instead of performing expensive DXA scans is described. The risk of fracture was estimated by maximum stress of the bone which was modelled as a parallel sided tube.

Grey-level profiles across the radius bone were sectioned into seven line-piece segments to create a model. The collected profiles were used to construct gender specific models from 68 male subjects and 48 female subjects. These models were used to interpret unseen images and locate the internal and external radius of the radius bone.

The internal and external radius were measured using the model-based interpretation. The error of the detection compared to manual measurements was less than 2%. The stress on the radius bone was derived, and used as a measure for the risk of fracture. Results showed a bivariate distribution of values between fractured and non-fractured subjects with 92% confidence in population different.

With further development this technique could be used to screen those at high-risk of a Colles' fracture by gauging the thickness of the wall of the radius bone using model-based image interpretation.

Keywords: Colles' fracture, risk of fracture estimation, distal radius bone, model-based interpretation.

ACKNOWLENGEMENT

This project would not have been possible without the support of many people. I would like to thank my supervisor, Mr. David Pycock for his support and encouragement throughout my M.Res and during the dissertation preparation. Also thanks to Prof D.W.L. Hukins, Mechanical Engineering, university of Birmingham who initiate the project idea and derived the first mechanical model for the failure of the radius in a Colles' fracture and Dr A Thomas of the Royal Orthopedic Hospital who provided medical advice and guidance.

I would like to thank Thai government for providing the financial support that made it possible for me to pursue the Master of Research programme in the UK.

Many thanks to Mr. Timothy Young-In Kim, Miss Anyaporn Sawasdichai, Korean and Thai friends in Bristol and Birmingham who offered a bedroom, a workplace, a laptop (when mine was broken), a friendly environment and other support whilst completing this dissertation.

The utmost thanks to my family and friends back at home in Thailand. I am very grateful to you all for being there for me. Despite the distance you always made me feel close to home. Finally, I am most indebted to my parents; Mom and Dad. I would not be here today without your belief in me and loving support. My profoundest thanks, and I would like to dedicate this dissertation to you both.

TABLE OF CONTENTS

LIST OF FIGURES

LIST OF TABLES

LIST OF ABBREVATION

aBMD	areal Bone Mineral Density
BMC	bone mineral content
BMD	Bone Mineral Density
DEXA	dual energy x-ray absorptiometry
CT	computed tomography
CI	Connectivity Index
H_A	Hole area
TBFF	trabecular bone filling factor
ASM	Active shape model
mlr	Maximum likelihood ratio
imlr	Inverse maximum likelihood ratio
PCA	Principal Component Analysis
PDM	Point distribution model

Mathematical symbols

r_i	inner radii
r_o	outer radii, radius radii.
Δr	cortical thickness
$\delta(r_o, \Delta r)$	risk of fracture function
$\varepsilon_{\max}$	maximum stress
μ	mean of grey-level profile in segment
σ	standard deviation of grey level profile in segment
l	segment length
η	segment slope
T	Training metric
x_s	the metric of parameters in a single profile
$\hat{\mu}$	Mean of parameters metric
Vs	Variance of parameters metric
$\hat{\sigma}$	Standard deviation of parameter metric
$\hat{x}_s^{'}$	Normalise the parameters metric

Units

SNR	signal-to-noise ratio
dB	decibel

1 INTRODUCTION

1.1 Colles' fracture

A distal fracture of the radius bone is a break of the forearm that is known as a Colles' fracture. It was defined in 1814 by an Irish surgeon and anatomist, Abraham Colles. This is a common fracture that can arise from a forward fall where the natural response is to reach out to break the fall. The Colles' fracture is also a common sporting injury. There are around 100,000 fractures amongst snowboarders each year in the UK (Hopson 2000; Hoynak 2000). Moreover, Colles' fracture is widespread amongst patients with osteoporosis (bone mineral loss state).

1.2 Colles' fracture treatment and recovery

Treatment of Colles's fracture is normally uncomplicated, simply requiring stabilization by a fitting device, such as a plaster cast, whilst the bone heals (Hoynak 2000). Occasionally surgery is needed to fit an internal traction device (Nelson 2005; Preston 2007).

Although the treatment is straightforward a Colles' fracture can be slow to heal. Initial healing can take six weeks and a further six to eighteen months may be needed for recovery (Hopson 2000). Discomfort is common throughout this time.

Most patients are able to resume light activities, such as swimming or exercising of the lower body, within two months of the plaster cast being removed or after surgical wounds have healed. Energetic physical activities such as skiing or football may not be possible for six months or longer (Hopson 2000). Unfortunately, normal muscle tone is never fully recovered.

1.3 Bone Mineral Density assessment

Bone mineral density (BMD) refers to the mineral content per cubic centimetre of the bone. It is used to diagnose osteoporosis and thereby predict the risk of bone fracture. The National Osteoporosis Foundation (NOF) recommends dual energy X-ray absorptiometry (DXA), which is a quick painless non-invasive method, to measure BMD.

Specific bones are scanned to measure the mineral density. The density is then compared to an average index based on age, sex and size of the bone. Data obtained from these comparisons are used to estimate the risk of fracture and the stage of osteoporosis. In general, a patient can expect to pay approximately £200 (in 2008) for a scan in private care.

Peripheral dual energy X-ray absorptiometry (pDXA), quantitative ultrasound (QUS), quantitative computed tomography (QCT) and peripheral quantitative computed tomography (pQCT) are alternative methods used to measure the bone density that predicts the risk of bone fracture. However, the results from these methods are less accurate compared to DXA.

1.4 Statement of problem

Since a Colles' fracture is common and the recovery period is extensive, it would be valuable if people at high risk of fracture could be identified and preventative measures taken. However as DXA scans are very costly, the prospect of a screening for the high risk of fracture is difficult.

Moreover, DXA does not assess structural factors related to the risk of a fracture and consequently cannot provide a reliable assessment of the risk of fracture. There may be other alternative methods to DXA which can give an estimate of risk fracture at a low cost of operation and can estimate the risk of fracture based on structural factors of the radius bone.

It is possible to measure the structural factors of the radius bone using a plain radiograph. The benefit of using a plain radiograph is the lower cost of operation. A plain radiograph is much cheaper than a DXA, which makes the prospect of a screening for the high risk of fracture possible.

It would be very beneficial if the risk of a Colles' fracture could be estimated by using radiographs. This would mean that existing X-ray systems with additional software would be sufficient to perform the procedure.

1.5 Aims

1. To investigate methods for estimating the internal and external diameter of the radius bone.
2. To investigate models to describe the grey-level profile of X-ray attenuation across the radius bone.
3. To evaluate an estimate of the stress that the radius bone can sustain and the risk of fracture.

2 LITERATURE REVIEW

In this chapter the structure of the radius bone is described and the use of BMD to estimate the risk of a Colles' fracture was reviewed. The use of image processing to assess the risk of a Colles' fracture from CT X-ray images was reviewed. This dissertation considered the use of a simple mechanical model of the radius and the use of a model-based image analysis to estimate the risk of a Colles' fracture. Therefore the basis of the mechanical model and model-based dimensional gauging was also reviewed.

2.1 The structure of the radius bone

The radius bone can be considered as a parallel sided cylindrical tube. Whilst the radius bone is not circular in a cross section but flattened on one side and not parallel sided this assumption has been considered appropriate by Langton (Langton 1996).

The radius bone contains two important components - the dense cortical surface layers and the trebecular central core. The cortical bone is a high density wall, contributing 80% of the weight of the bone (Roylance 2000; Nelson 2005). The trabecular region of the bone is low density osseous tissue. The densities of these layers contribute to the mechanical properties of the radius bone.

A model of the hollow tube with an internal radius (r_i) and an external radius (r_o) is shown in Figure 2.1. The issues that need to be investigated are the appropriateness and the accuracy of the mechanical model. We also need techniques that can measure the internal and external radius in order to estimate the stress that can be born.

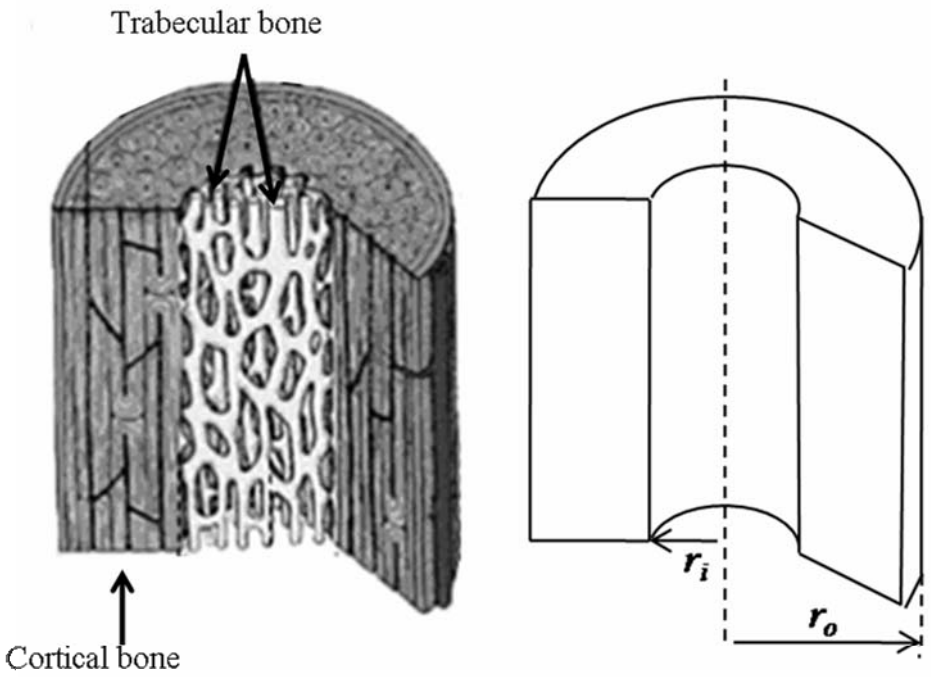

Figure 2.1 Mechanical model of radius bone, taken from Langton (Langton 1996).

2.2 Bone strength estimation

Bone strength can be estimated by measuring the bone mineral density (BMD), commonly reported as an average density (g/cm²) and evaluated as the population T- and Z-score. T-score indicates the deviation of BMD from the mean bone density of a healthy 30-year-old adult. The Z-score is a measure of the deviation of BMD from the age dependent population average. Figure 2.2 shows the T-score (strong line) and Z-score from age 20 to 100 years.

The bold band in Figure 2.2 is the ±1 SD limit about the population average. For example a subject at age 60 (shown as a dot in Figure 2.2) has T-score = -2.0 and Z-score = -0.5. This means the subject has a much lower BMD compared to a 30-year-old but the BMD is close to the age related average, with a Z-score of 0.5.

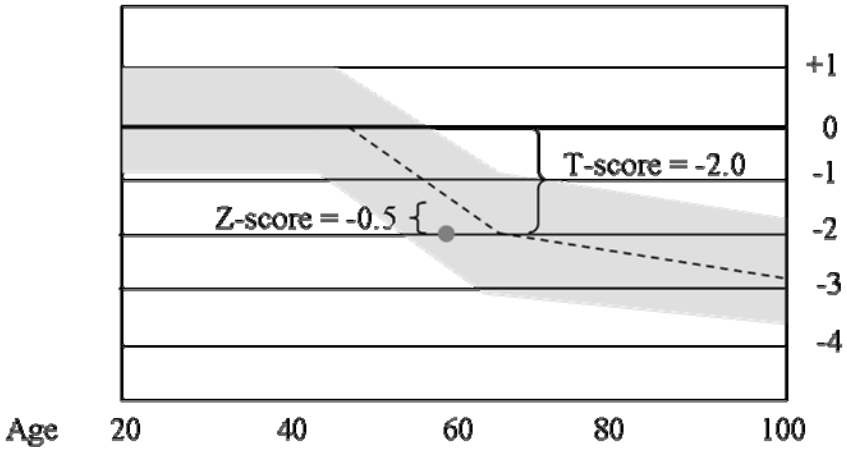

Figure 2.2 The assesment of BMD by T-score and Z-score.

An estimation of BMD is widely used to measure the bone content in a particular site of the body. The risk of a bone fracture is estimated on the basis that the strength of the bone is related to the mineral density in the bone (Hopson 2000). Table 2-1 shows BMD categories of assessment for postmenopausal women and men aged 50 or over.

Table 2-1 T-score scores and BMD category

T-Score	**BMD category**	**Treatment**
≥ -1	Normal BMD	Medication not normally required
-1 to -2.5	Low BMD (Osteopenia)	May need to take osteoporosis medication
≤ -2.5	Osteoporosis	Should take osteoporosis medication

BMD measurements require a careful calibration the object size, geometry and the distribution of X-ray densities in an object can affect the BMD values, caused by beam hardening and Sigmoid surface density gradient (Hopson 2000).

Several works (Lee *et al.* 2007; Gordony *et al.* 1998) have estimated the risk of Colle' fracture using image processing methods, rather than measuring BMD. Lee (Lee *et al.* 2007) proposed a measurement called Trabecular Bone Filling Factor (TBFF), representing the volume of a trabecular bone.

In their experiment, radiographic system of DXA was calibrated using an aluminium step-wedge. BMD was measured by a radiographic attenuation with a fixed exposure of 51kVp at 5mA.

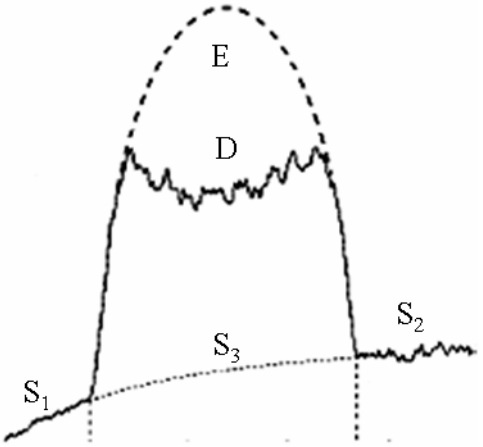

Figure 2.3 Grey-level profile across the radius and interpolated curve E and S3, taken from Lee's result (Lee *et al.* 2007).

An X-ray attenuation profile across the radius taken from Lee's experiment (Lee *et al.* 2007) is illustrated in Figure 2.3. The attenuation profile is modified by subtracting density values extrapolated across the bone. The dotted curve, E, is an extrapolation of the attenuation due to the cortical bone and S_3 is an interpolation of the attenuation due to soft tissue (S_1 and S_2).

Lee estimated the TBFF by using a ratio between trabecular bone content and full-filled bone density. The trabecular bone content was estimated as the difference between the area under curve E and curve S3. The full-filled bone content was calculated as the difference between the area under curve D and curve S3. Results showed a linear correlation between the TBFF and BMD of 0.87 and a tentative estimate of reproducibility error of 3%.

An estimation of bone loss which is provided by the density of trabecular bone can indicate bone content density (Hopson 2000), however, a theoretical link between TBFF and BMD cannot be found in Lee's work.

Gordony (Gordony *et al.* 1998) proposed other measures to estimate the structural strength of the radius bone, called Connectivity Index (CI) and Hole Area (H_A). Gordony used high-resolution computed tomographic (CT) images to analyse the micro-structure of the radius bone.

Marrow pore size can be assessed using a binary image of a CT X-ray, as shown in Figure 2.4 (a). A 8-connected region growing algorithm was used to grow each pore to find the average area of the marrow pore size – Hole Area (H_A). CI can be assessed by using a skeleton image as shown in Figure 2.4(b) as the micro-structure strength can be considered by assessing network connectivity of the trabecular layer (Cann and Genant 1980).

CI was proposed to represent network connectivity as:

$$CI = \frac{Nd - Fe - Ip}{Nl} \times 100$$

Nd the junction between three or more structs (an element in a skeletal image) is defined as a node

Fe A struct that is connected at one end and is free at the other end

Ip isolated points

Nl network length

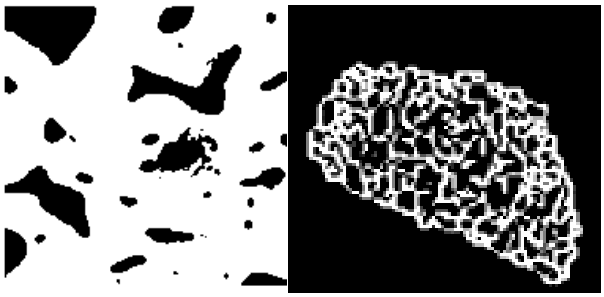

(a) (b)

Figure 2.4 (a) the binary image of the marrow pore and (b) skeleton image of a cross-section of a bone, taken from Gordony's result (Gordony *et al.* 1998).

The results showed that there was a strong linear correlation between BMD and CI ($r > 0.9$) and a moderate correlation between BMD and H_A ($r \sim 0.77$). The measurements were shown to be reproducible, changing within 1% when the region of trabecular bone changed by 20%. However, the dependence on CT imaging to analyse micro-structure makes this a high cost procedure.

Muller (Muller *et al.* 2008) studied the mechanical properties of the distal radius bone to find a relationship between failure load and cortical thickness. The mechanical properties of thirty-two human radius bones were assessed using different techniques. For example, cortical thickness was measured by peripheral quantitative computed tomography (pQCT) in single slice scan (thickness of 1mm is equivalent to pixel size of 0.2mm). Failure load was assessed using a mechanical testing machine; the specimens were subjected to quasi-static compressive mechanical stress until the sample failed. The best correlation to failure load was provided by cortical thickness, predicting 52% of the failure load variability.

Another approach to estimating the risk of structural failure from a mechanical model is provided by Xue (Xue *et al.* 2002). They studied the deformation of a long cylindrical shell subjected to external pressure. A hollow cylinder was applied to boundary condition of Euler-Bernoulli beam equation using finite element analysis to observe the deformations of material shape, stress obtained and the load failure. The study showed that a 2% change of shell thickness can sustain a 33% increasing of the external pressure.

A mechanical model to estimate the risk of fracture can be derived from Euler-Bernoulli beam equation. However, the issues that need to be investigated are the adequacy of the mechanical model and the accuracy of dimensional gauging in the plain radiographs.

2.3 Locating boundaries between the radius bone margins

An accurate estimate of the internal and external radius is necessary to measure the risk of fracture. The edge at the internal margin is not well defined because the grey level profile is a ramp and has no discontinuity to indicate a position of the edge. Therefore a novel strategy is needed to locate the position of the edge.

Peter (Peter *et al.* 2008) proposed a watershed algorithm to cluster the pores in high resolution CT images of a trabecular bone so as to measure the thickness of the pore regions. Region growing was used to separate the pores from each other. Neighbouring pixels of the pores were merged together if their grey-levels were similar.

Figure 2.5(a) shows the segmentation result. Blurred boundaries between pores can be separated using a distance map. Non-critical threshold was used to bisection between pores and the trabecular region. This is possible as the difference of grey-level profile between the trabecular region and the pore area is almost 100 levels as seen in figure 2.5(b), which is sufficient to differentiate between the two.

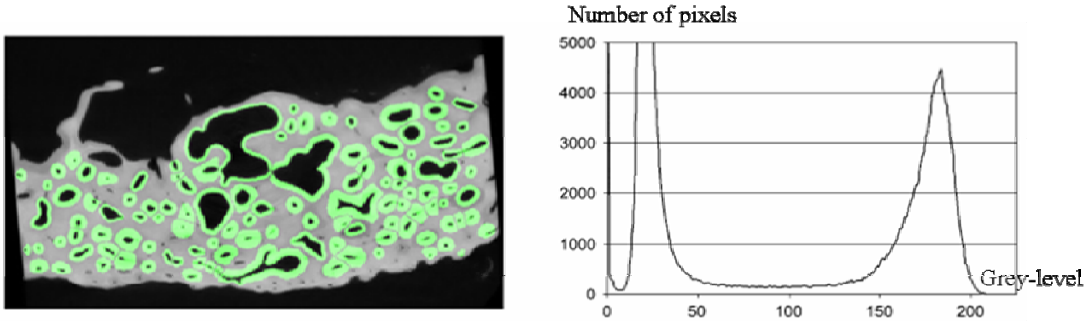

(a) (b)

Figure 2.5 (a) the region thickness of the pores (b) a histogram of CT-image showed grey-level difference between pores(the first peak) and trabecular region(the second peak), taken from Peter's work.

Saparin (Saparin *et al.* 2006) studied a segmentation technique to identify the boundary between the cortical and trabecular layers in pQCT images. They used a band threshold,

which relied on the mean and the standard deviation of the pixel values inside a pre-defined trabecular region, to identify the boundary.

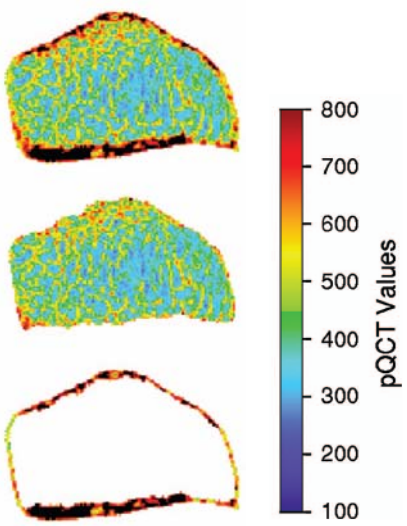

Figure 2.6 the trabecular-cortical bone is separated by band thresholding, taken from Saparin (Saparin *et al.* 2006).

The difference between the pQCT values of the cortical and trabecular bone is shown in Figure 2.6. The gap between these regions is wide; therefore, a band threshold is adequate to separate these regions from each other.

The two studies sought to segment the regions in a high resolution image with a substantial grey-level difference. However, the grey-level difference between the cortical and trabecular region in a radiograph is not well defined. The boundaries are weak and difficult to detect by region growing, grey-level threshold and common edge detection algorithms.

Graham *et al.* (Graham *et al.* 2000) studied a statistical edge detection to locate weak boundaries in the radiographs. They examined the use of different statistical measures applied using a sliding dipole. They undertook a systematic test of operator responses to a step edge in noise, varying the step size, noise level and size of the dipole sample region.

They compared the performance of the operators with the Canny operator (Canny 1983) on both synthetic and natural images - radiographs of replacement hip joints. The result showed that statistical edge operators detected or performed well compared to the Canny operator, producing a promising response on the natural images where the Canny operator had failed. The best response was given by the standard deviation difference (E_{SD}), which is computed by:

$$E_{SD} = 2\,\sigma_{AB} - (\sigma_A + \sigma_B)$$

Where σ is the standard deviation of population

This was derived by replacing entropy terms with the difference in the standard deviation between two populations, A and B. The advantages of E_{SD} as a detector of weak boundaries are that it is sensitive to weak edges, noise resilient and has a low computational cost (Graham *et al.* 2000). Nevertheless, there is no theoretical basis for replacing entropy with standard deviation in this formulation.

There have been several studies (Azzopardi *et al.* 1996; Pitas and Venetsanopoilos 1986; Chalana *et al.*1997) for the use of maximum likelihood as an edge detector. The theoretical basis for the maximum likelihood formulation of edge detection is derived from the analysis of the likelihood that two samples are taken from similar or dissimilar populations as summarised in the following.

Assuming that two populations have a Gaussian probability distribution, i.e.:

$$P(x) = \frac{1}{(2\pi)^{\frac{d}{2}}\left|\sum\right|^{\frac{1}{2}}} e^{\frac{1}{2}\frac{(X-\mu)^t(X-\mu)}{\Sigma}}$$

Where: $P(x)$ is the probability of drawing a particular value for sample x from the population.

μ is the mean of the population

Σ is the covariance of the population

X is the sample vector from which x is drawn.

d is the sample size

This is the description of multivariate Gaussian probability distribution. The likelihood ratio between two populations A and B is:

$$LR\left(x|\theta_A\theta_B\right)=\prod_{n_1}P\left(X_A\right)\prod_{n_2}P\left(X_B\right)$$

The likelihood that a particular value of x is drawn from the population of AB is:

$$LR\left(x|\theta_{AB}\right)=\prod_{n_3}P\left(X_{AB}\right)$$

Where n_1, n_2 and n_3 are the population sizes of A, B and AB.

When the two populations A and B are the same with Gaussian distributions then the population AB will also be Gaussian distributed. If the populations A and B are Gaussian distributed but from different populations then the distribution for AB will not be Gaussian distributed. The ratio of likelihood ratios provides a normalising factor and is:

$$\frac{LR\left(x|\theta_A\theta_B\right)}{LR\left(x|\theta_{AB}\right)}=\frac{\prod_{n_1}P\left(X_A\right)\prod_{n_2}P\left(X_B\right)}{\prod_{n_3}P\left(X_{AB}\right)}$$

$$\frac{LR\left(x|\theta_A\theta_B\right)}{LR\left(x|\theta_{AB}\right)}=\frac{\left[(2\pi)^d|\Sigma|\right]^{-\frac{n_1}{2}}\left[(2\pi)^d|\Sigma|\right]^{-\frac{n_2}{2}}}{\left[(2\pi)^d|\Sigma|\right]^{-\frac{n_3}{2}}}$$

Substituting for $n = n_1 = n_2 = \frac{1}{2}n_3$, the ratio of likelihood ratios becomes:

$$mlr=\frac{\left|\Sigma_{AB}\right|^2}{\left|\Sigma_A\right|\left|\Sigma_B\right|}$$

For a univariate distribution this reduces to:

$$mlr = \frac{\sigma_{AB}^2}{\sigma_A \sigma_B} \quad (2.1)$$

The maximum likelihood ratio (*mlr*) can be used to identify the points that divide statistically distinct populations. However, the unbounded nature of the ratio of likelihood ratios makes it difficult to ascertain when a significant change occurs. This problem is avoided if the inverse of the ratio of likelihood ratios is used. This measure varies between zero when the samples come from different populations and 1 when the populations are the same. The inverse maximum likelihood ratio is:

$$imlr = \frac{\sigma_A \sigma_B}{\sigma_{AB}^2}$$

As the variance of AB increases with respect to that for A and for B, the *imlr* value decreases, signifying the presence of an edge. If the distributions are non Gaussian, the same changes will take place although the measure of likelihood might be inaccuracy. Therefore, the requirement for a Gaussian distribution is not strict, given that it is the change in *imlr* value is important.

The size of the operator was able to affect to the boundary of maximum likelihood profile. There is a balance required between having a statistically adequate number of samples and suitable sizes to localise edges precisely which can be found experimentally.

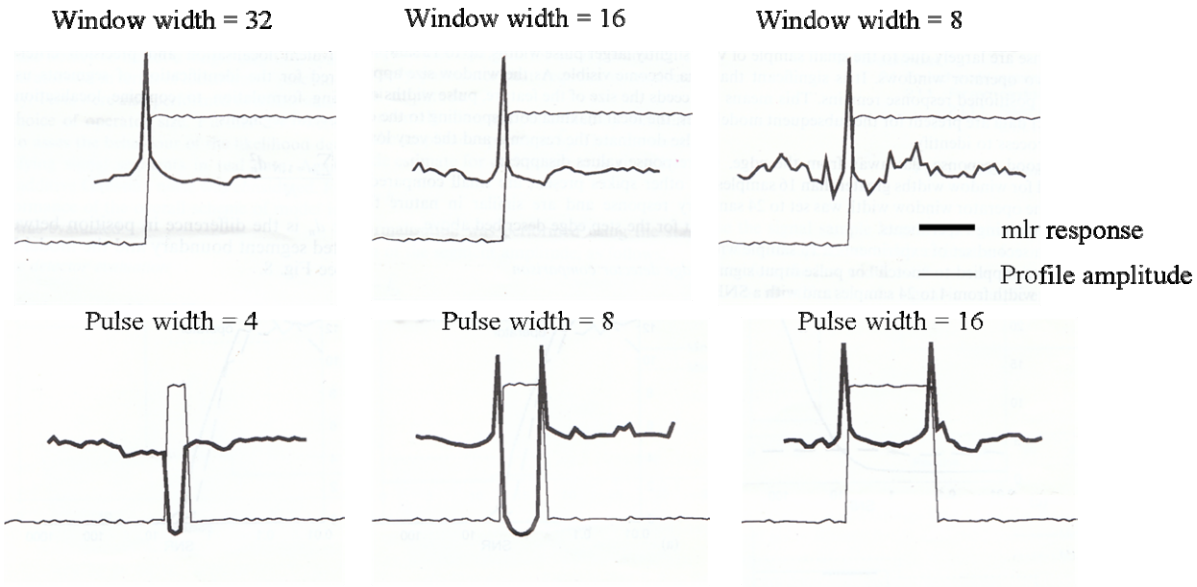

Figure 2.7 (a) maximum likelihood ratio response when the size of the neighbourhood is changed (b) the shape of maximum likelihood ratio when the region width is changed (windows size = 16), taken from Pycock's study (Pycock *et al.* 2000).

Pycock's study (Pycock *et al.* 2000) showed a relationship between the window width and operator response. Maximum likelihood ratio showed a marked variability in the response away from the edge when a small window was used. The response was smoother when a larger window size was used, as shown in Figure 2.7(a). A good response was obtained with a window width greater than 16 samples.

Figure 2.7(b) shows the effect of pulse width on the mlr response. The operator could not detect the edges of a pulse that was much smaller than the width of the operator window. The results also showed a local minimum when the pulse width was half the window size. The operator was able to respond efficiently to edges when the pulse width was greater than 75% of windows size.

Edge uniformity should also be considered. If edge is perpendicular to the scan line, square windows (n x n) as shown in Figure 2.8 (a) can create a good response. When the boundary is curved with a radius that is small compared to the region size then the edge position is likely

to be displaced from the position of the edge along the centre line of the operator; the shaded and non-shaded regions would not be separated ideally as shown in Figure 2.8(b). In this circumstance a narrower rectangular, window (w x h) as in Figure 2.8 (c), could be used to improve the result of edge detection (Graham *et al.* 2000).

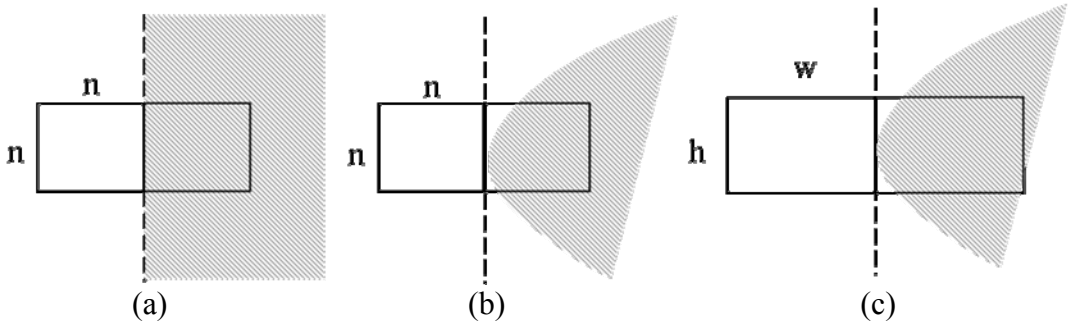

Figure 2.8 (a) uniform boundary with square window (b) non uniform boundary with square window (c) non uniform boundary with rectangular window

The issues that need to be examined are:

1. Does the maximum likelihood ratio detect the true edge position?

2. Is the maximum likelihood ratio effective at detecting low contrast edges?

3. What is the shape of maximum likelihood ratio response for a grey-level profile across the radius?

2.4 The uses of model interpretation

To measure the bone thickness using a model requires a reliable and repeatable technique. We also need an algorithm that is fast and robust to radiographs from routine collections.

The point distribution model (PDM) is a statistical representation of a shape. The model is obtained from a training set of labelled images. Principal component analysis (PCA) is used to determine the mean object shape, and modes of shape variation.

To train the model landmarks, several images are adjusted to the same orientation and scale since the order of landmarks need to be the same as that of the model. As the manual indication of landmarks is a time consuming and tiresome task, most researchers have developed an automatic tool to assist in this procedure. Figure 2.9 shows a sample of PDM with 32 landmarks.

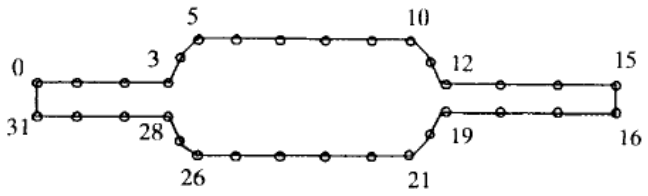

Figure 2.9 A resistor PDM has 32 landmarks, taken from Cootes (Cootes *et al.* 1993).

It is important to have a statistically significant number of samples to define a stable model that captures the range of variation in the form of the object; for example Cootes (Cootes *et al.* 1993) used a training set of 300 labelled samples in face recognition.

The mean PDM model must be scaled, rotated and translated to fit the pose of the landmarks of an unfamiliar image; otherwise the model cannot match efficiently (Cootes *et al.* 1993). PDMs cannot support a large degree of bending as it showed a distorted shape matching result (Lanitis 1993; Cootes 1993). This can be a problem where medical images are concerned because there is considerable scope for biological variation and this can include bending which cannot be modelled in a PDM scheme.

The Active Shape Model (ASM) exploits the use of PDM landmarks. In ASM the mean shape is transformed by translation, rotation and scaling of landmarks. The shape is adjusted iteratively to fit the model. To locate a new landmark a search is performed to find the strongest edge along the normal to the initial boundary path, shown in Figure 2.10(a).

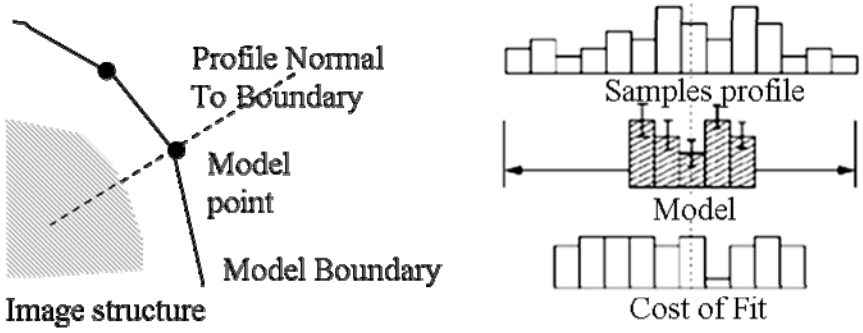

(a) (b)

Figure 2.10 (a) Normal to the initial boundary (b) A search along sampled profile to find best fit to the grey-level model

The Manhalanobis distance is used to find the best fit of the model to the revised landmarks that are on either side of the model point.

Shape deformation is only allowed in a perpendicular direction to the shape. This can be a problem if there are, for instance, few normal lines in a particular direction (Cootes *et al.* 1993). The deformation will have difficulties in moving in the direction and the problem is worsened if the boundary is not well defined at the edge of a profile.

An ASM needs a closed boundary representation (Cootes and Klim 1995) otherwise the deformation direction of the model might be misinterpreted. Where this investigation is concerned a radiograph of the radius will not provide a closed boundary.

Pycock (Pycock *et al.* 2000) studied the use of a model-based profile interpretation in order to identify 6 different classes of radar signal. They used a piece-wise model to describe the signal by breaking the signal into several segments as shown in Figure 2.11. Breakpoints of the signal profiles were detected by an edge detection algorithm. To train a profile model, these breakpoints were chosen to be the division points between segments in the profiles and the segment width and average amplitude were used as segment parameters.

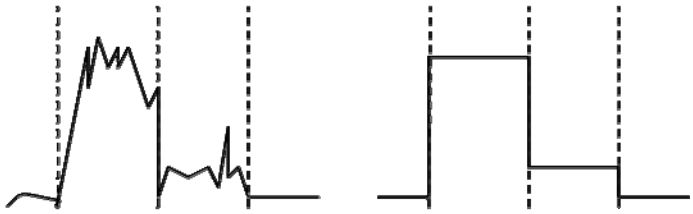

Figure 2.11 Piece-wise segment model

A model is described by the mean and standard deviation of the segment parameters. A low standard deviation for the parameters of a model indicates that a good match to these parameters is required. A probabilistic metric was used to identify how well the interpretation matched the model.

The metric was used was:

$$P_{match}(\bar{x}) = \frac{\exp\left(-\frac{1}{2}(\underline{x}-\underline{m})^T S(\underline{x}-\underline{m})\right)}{(2\pi)^{\frac{1}{2}}\det(S)}$$

Where x is the vector of segment parameter values, $\underline{m}$ is the vector of model parameters values and S is the model covariance matrix.

An exhaustive search is a primary search technique that was used to find a solution in the probabilistic metric. An exhaustive search selects all possible combinations to consider the best match to the model. Some of these combinations can be eliminated at an early stage because they do not provide a sufficiently close match, at an early stage of the interpretation to be plausible. When the number of possible candidate segments increases, the combinations and the cost of evaluating all options is prohibitive and increases exponentially.

In dynamic programming only the best matches at an early stage are pursued. This dramatically reduces the number of combinations that must be considered. The only requirement is that an initial decision on the best match does not depend on later decisions. A

heuristic criteria is required that will provide a measure of the goodness of the match. Heuristic criteria can be used to prune the search space of dynamic programming so that a polynomial dependence on the number of candidates operates.

Pycock (Pycock *et al.* 2000) used a heuristic search to merge candidate points of a amplitude profile of radar signal to fit the model. The candidate points are merged together if they give a better match than not being merged; comparisons are made by determining the probabilistic metric. The breakpoints that have been merged will never be used again since it is impossible that one breakpoint can be a part of two segments.

The largest danger is that this approach might lead to a locally optimal solution that is not close to the globally optimal solution being sought. To reduce the possibility of a local minimum being found care is needed in the design of cue generation so that a sufficient number, but not too many cues are generated.

Modelling a bone profile is possible and this requires only one dimensional data, a grey-level profile, not two dimensional data as for the ASM. However, it is important for consistency in the training sample and between the training and interpretation that profiles are taken from the same position on the radius bone; for example Muller (Muller *et al.* 2008) used a position at one-third of the length of the radius bone for making measurements in their experiments.

2.5 Cue generator

A cue generator is the process of finding clues to represent an image, or a profile. For model-based interpretation these clues should be landmarks, which can be located by a peak detection algorithm.

A common problem in peak detection is the over generation of peaks caused by local minima. A smoothing technique can be used to reduce the number of local minima by applying an average mask to the original profile. However, the profile can be changed by smoothing and the peak of the profile can be shifted from P to P' as shown in Figure 2.12.

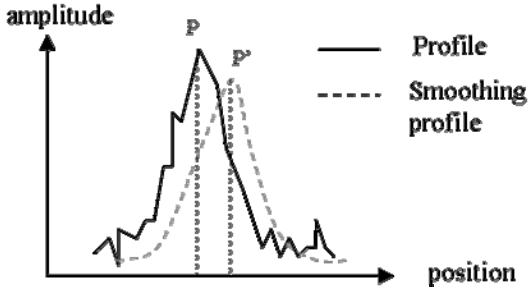

Figure 2.12 Peak shifting caused by smoothing from P to P'.

Curve fitting can be used to locate the actual peaks and avoid the local minima. The equations such as polynomials can be applied to fit a profile. If the curve is of an appropriate order, the peak from this technique must be accurate because it is the best match between the profile and the equation. However, the difficulty of curve fitting is finding the suitable equations which might be variable or cannot be found. The candidate equations normally are 2^{nd}, 3^{rd} or more order of polynomials and to fit these equations is a time consuming task for the peak detection algorithm.

Morphology operator can be also used to avoid the local minima. Top-hat transform is a morphologic operator developed by Meyer (Meyer 1979) to extract the detail that differs from the background. The transform is given by the subtraction of opening of an image (or profile) from the image (or profile) as expressed here:

$$T_w(f) = f - f \circ b$$

Where f is image function, b is structure element, o is opening operator and T_w is top-hat transform function.

The size of the structuring element is important. If it is too small, background removal is affected by a presence of random noise; if it is too large, it cannot reproduce the small scale variations of the features sought, therefore, a good compromise has to be found. The top-hat transform is capable of extracting strong peaks. The structure element opened the profile, in which local minima were simultaneously erased if they are smaller than the size of the structure element as shown in Figure 2.13.

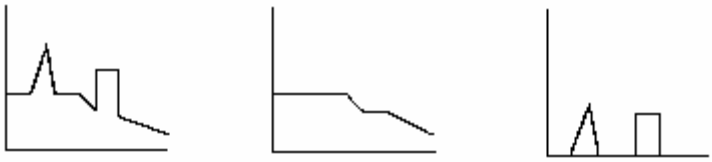

(a) (b) (c)

Figure 2.13 (a) original profile (b) opened profile (c) top-hat transform

An alternative technique to reduce the number of local minima is non-maxima suppression. Non-maxima suppression considers the profile along the gradient direction. Pixels that are not at the peak (non-maxima), are deleted. Therefore, the real peaks in profiles are shown in non-maxima suppression. Thresholding may be applied in order to locate the positions of the peaks.

A hysteresis system has been introduced to solve the peak detection problem. To detect the peaks, positions with the amplitude higher than peak high (h) are candidates. However, the position will be selected as a peak only if it has the highest amplitude within a range of peak-width (w).

Peak detection with hysteresis can avoid local minima. It is also a rapid process compared to top-hat transform or non-maxima suppression and the profiles are not changed by the algorithm. The detection is also flexible to the peak width and peak height, only defining parameters w and h to the algorithm is necessary. To uses the hysteresis system to detect peak

in the grey-level profiles of the radius bone, we have to consider the parameters (w and h) to guarantee their as many potential peaks can be detected as possible.

2.6 Theoretical basis of bone fracture

The distal radius bone is broken by the impulse force which arises from a change of momentum. The impact of this force can be analysed to estimate the risk of fracture as following.

Bone fracture can be analysed by a failure of the beam buckling. The parameters used in the analysis were the inner radius (r_i), the outer radius (r_o) and the length of the bone (L). The momentum changed, depending on the external force P is shown in Figure 2.14.

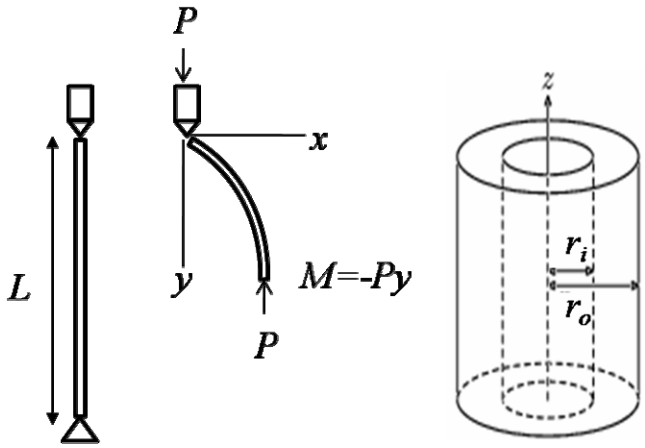

Figure 2.14 (a) beam buckling (b) a beam mechanical model

With the first mode of buckling, the critical force before the beam loses stability (P_{Crit}) is given by:

$$P_{Crit} = \frac{\pi^2 EI}{L^2}$$

Where

E Modulus of elasticity

L Length

I moment of inertia

Moment of inertia of a hollow cylinder in the x-axis and y-axis is:

$$I_x = I_y = \frac{1}{12} m\left[3\left(r_i^2 + r_o^2\right) + L^2\right]$$

The force to the distal radius is correlated to body mass (W). The bone will be broken when:

$$W > P_{cr}$$

The estimation requires r_i, r_o, L, W and E in order to determine the risk of fracture. It is possible to measure E by the change of velocity of ultrasound in the bone (Greenfield *et al.* 1981). r_i and r_o can be measured from radiographs but L may be unavailable from a routine scan.

The risk fracture can also be estimated by a failure of beam bending, using the maximum bending stress in a tube. The Euler-Bernoulli equation is given by:

$$\varepsilon_{\max} = \frac{M r_o}{I}$$

where

$$I = \frac{\pi\left(r_o^4 - r_i^4\right)}{4}$$

r_0 the external radius

r_i the internal radius

ε the maximum stress

The risk of fracture is proportional to:

$$\frac{4 r_o}{\left(r_o^4 - r_i^4\right)}$$

i.e.

$$\frac{4 r_o}{\left(r_o - r_i\right)\left(r_o + r_i\right)\left(r_o^2 + r_i^2\right)}$$

The risk of fracture (δ) depends on:

$$\delta(r_o, \Delta r) = \frac{1}{r_o^2 \Delta r} \tag{2.2}$$

where $\Delta r = r_o - r_i$

The function for estimating the risk of fracture depends on the inner and outer radius of the tube. The derivation function as in the following equation showed that the risk of fracture estimation depends on the inverse square of the outer radius of the tube. This was fully analysed in Appendix A.3.

$$\frac{\partial \delta}{\partial r_o} = \frac{\ln(\Delta r)}{r_o^2} + \frac{2}{r_o \Delta r} \tag{2.3}$$

Risk estimation using the bending approach has been adopted as it was able to apply on a fewer parameters than the buckling approach. Only r_i and r_o are needed to be measured in order to estimate the risk. However, the derivative function showed that the risk of fracture by bending is very sensitive to the change of r_o and Δr therefore we need to ensure that this risk estimation has potential to differentiate the high risk samples from the low risk ones in order to show the reliability of the measurement.

Lee (Lee *et al.* 2007) showed the reliability of their measurement by assessing r-square between the TBFF value and BMD, which is costly, from the same position of the bone samples. Gordony (Gordony *et al.* 1998) studied the micro-structure parameters (CI and H_A) and showed the reliability of their parameters by showing the gap of assessed values between fractured subjects and non-fractured subjects. Figure 2.16 showed the gap difference of CI. The graph showed that a line -2 SD from the mean values of non-fractured subject has a potential to differentiate subjects with a high risk of fracture from those with a low risk without BMD assessment.

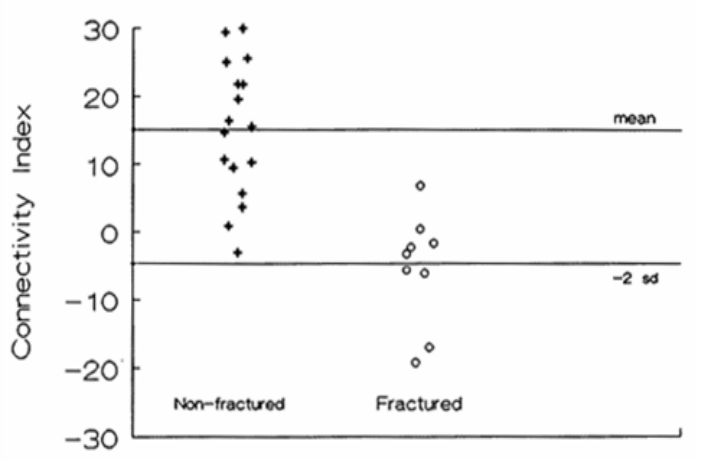

Figure 2.15 A bivariate display of connectivity index assessment between non-fractured and fractured sample.

The line ±2sd is a good criterion if the data distribution is Gaussian as 95% of population is covered within ±2SD from the mean of data. An issue that need to be investigated is the efficiency of the separation line ±2SD in this project or which criteria can be used to distinguish the high risk samples from the low-risk ones.

2.7 Summary

The trabecular filling factor (Lee *et al.* 2007) used an interpolation of the grey-level profile across the radius to estimate the mass of trabecular bone. CI and H_A (Gordon *et al.* 1998) used image processing to analyse the internal parameters of the trabecular bone which provides an estimation of bone strength. These parameters showed a strong correlation to BMD (Lee *et al.* 2007; Gordon *et al.* 1998); however, there are few evidences that showed that how these parameters are involved theoretically with the risk of fracture.

An estimation of the risk of fracture using a mechanical model is possible. The well known Euler-Bernoulli beam equation can be applied to estimate the risk, however, the issues that need to be investigated are the adequacy and the accuracy of the mechanical model.

An estimation of the bone thickness is another aspect to be calculated in order to obtain an accurate mechanical model. The questions that need to be answered are which ranges of the grey-level profile of the bone can be measured as the thickness of the bone and as the boundaries between the cortical and trabecular layers are weak, how to measure the thickness of the bone from a plain radiograph with accuracy.

Many techniques were reviewed to detect the boundaries between cortical and trabecular layers in the radiographs. Basic segmentation techniques such as region growing, thresholding or watershed-segmentation have difficulty in locating the weak boundaries of the radius margin. Statistical edge detection such as E_{sd} and *mlr* showed a promising result in indicating the weak boundaries in medical images. We need to study whether the *mlr* is suitable for edge detection and whether it has potential to identify the weak boundaries in the grey-level profile across the radius bone.

ASM is a powerful technique used for highly variable completed shapes but in this case it is difficult to get a full-length image of the radius bones since the scan was performed partially. This means that the model will lack stability and will too readily permit an inappropriate interpretation.

However, it is possible to model a grey-level profile across the radius instead of the bone shape. The important issues that need to be investigated are:

1. How to describe a grey-level profile across the radius with a model?
2. Where the profiles on the radius should be collected?
3. How to determine which parameters are suitable for interpreting the profiles?

A review of cue generation showed that smoothing can reduce a number of unnecessary candidates by removing the local minimum from the profile; however, this process caused the

position of the peak to change. A curve fitting can also be used to detect the peaks but it is a slow and computationally intensive algorithm.

Top-hat transform and non-maxima suppression are less complicated than curve fitting. They also have a potential to decrease the number of local minimum, however, these methods require some techniques to locate the position of peaks.

Peak detection with hysteresis can avoid local minima, run fast and locate the peaks without the profile changed. The detection is also flexible to the peak width and peak height. However, we have to examine the parameters (w and h) to ensure that they would match the peaks of the grey-level profile across the radius bone.

A deformation of the bone to determine the risk of fracture can be analysed by two approaches, buckling and bending. In this circumstance, the buckling approach cannot be carried out because of the unavailability of the data and facility limitations.

It was shown that equations used in the bending approach are sensitive to the change of bone thickness. However, this can be resolved by an appropriate design of measurements of the bone thickness. Experiments that evaluate the measurements are needed. Moreover, the risk of fracture from the bending approach needs to be examined to ensure that it is sufficient to differentiate between the high risk and the low risk of fracture samples.

3 METHODOLOGY

The risk of fracture estimation was derived by using a bending moment equation based on a hollow cylindrical model. The internal and external radius of the trained model was measured in order to estimate the risk.

This chapter shows radiographs, categorised for training and testing, and the details of the methods and strategy of training and interpretation of bone profiles and also the implementations of experiments.

3.1 Materials

3.1.1 Radiographs

A hundred 16-bit radiographs, collected from a routine procedure, were categorised for training and testing. Patient identifications were removed from the radiographs. The radiographs had varying levels of opacity as shown in Figure 3.1. The X-ray exposure, energy and geometry were not available to be controlled, nor was it possible to perform calibration measurements.

Figure 3.1 An illustration of the variance in the opacity of the radiographs used in this project.

3.1.2 Software in experiments

Training and interpretation programs were written in Java language using Netbeans IDE 6.1 with Java development kit 1.6.0. Experimental data was recorded and analysed by functions

within Microsoft Excel 2003 and MATLAB 6.5. ImageJ 1.40g was used to observe and manipulate the radiographs.

3.1.3 Bone Profiles

Grey-level profiles and maximum likelihood ratio of the profiles were collected from the radiographs and saved as ASCII files with filename extension ".pro" and ".mlr" respectively. Approximately 100 grey-level profiles were taken at a fixed position on the radius bone, as shown in Appendix A.1. Each profile consisted of roughly 150-200 integer data values.

Of the radiographs not showing a fracture 68 were analysed separately from male subjects and 48 from female patients. Figure 3.2(a) showed the grey-level profiles from 25 male and 25 female subjects; these profiles were used to train the bone profile model for each gender. Figure 3.2(b) shows grey-level profiles taken from the radiographs of 43 male and 23 female subjects to form the test data.

Grey-level profiles taken from radiographs of 9 male and 8 female subjects who had experienced a wrist fracture were also categorised to assess the risk of fracture.

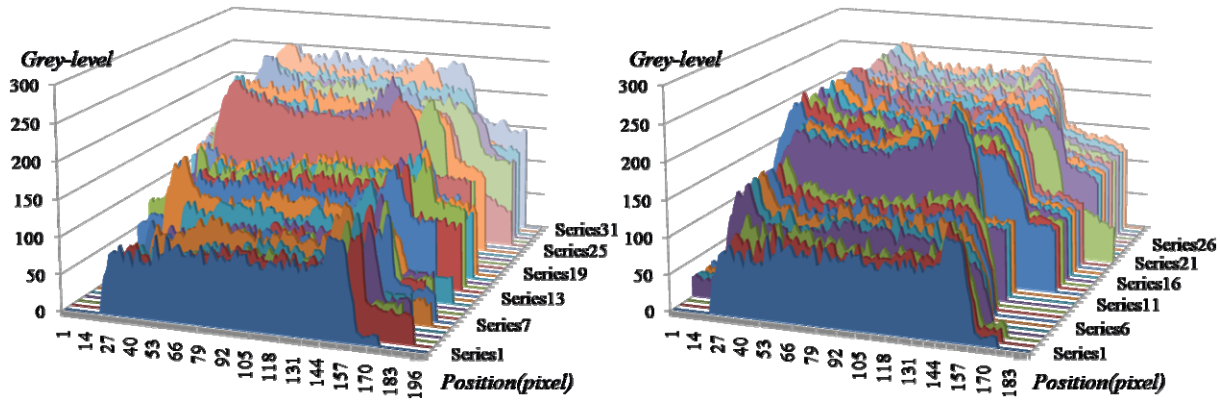

(a) (b)

Figure 3.2 Grey-level profiles (a) training set (b) test set.

3.2 Methods of model-based interpretation

3.2.1 The scheme of model interpretation

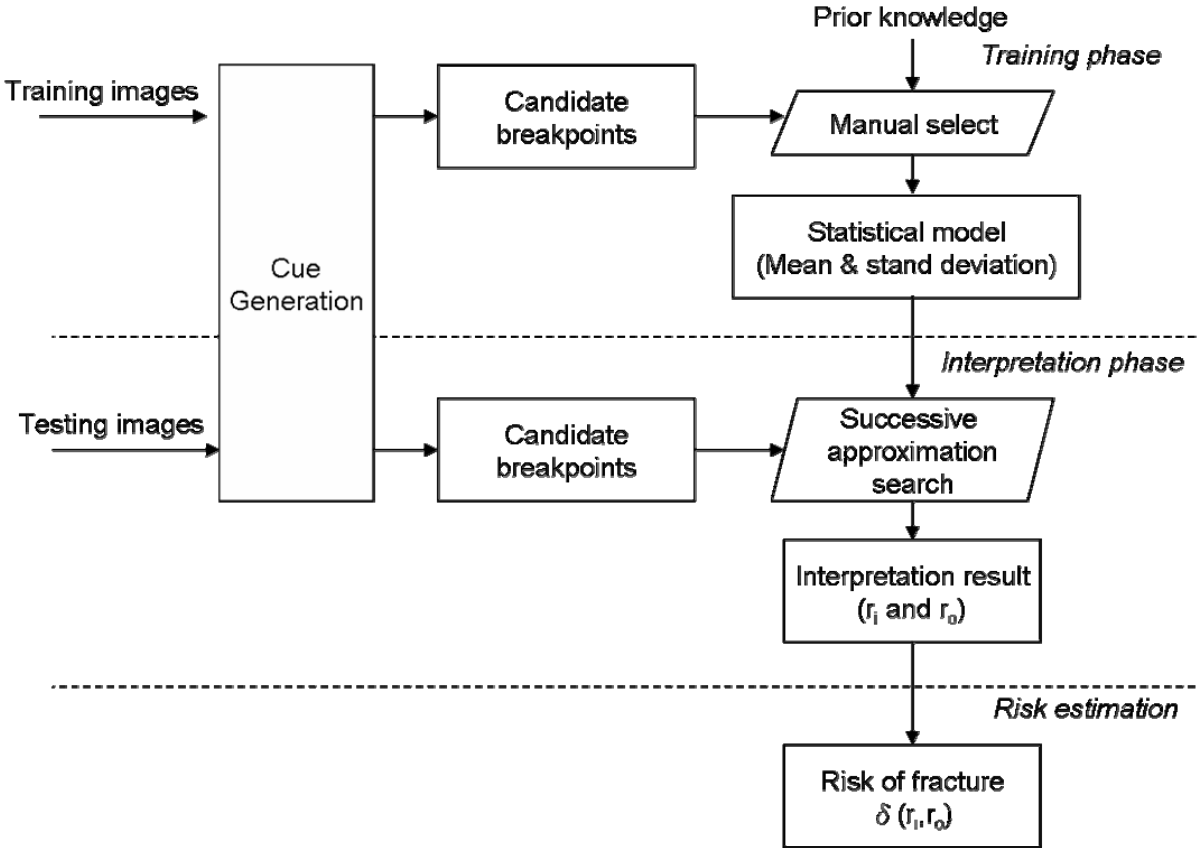

Figure 3.3 Schematic diagram of training, interpretation and risk estimation

1) Training — the phase in which a model is trained by selecting a series of landmarks on profiles (from candidate breakpoints).

2) Interpretation — the phase in which the statistical model of the training data is used to interpret unseen data. The outcomes of the interpretation are the internal radius (r_i) and the external radius (r_o) of the radius bone.

3) Risk estimation — the process of evaluation of model-based interpretation using bone thickness to assess the risk of fracture (δ).

Candidate breakpoints were extracted using a cue generation algorithm that provided a choice of landmarks for both training and interpretation phases.

3.2.2 The description of piece-wise model and parameters

Grey-level profiles across the radius bone were extracted from the radiographs as shown in Figure 3.4(a). The extracted grey-level profile and a piece-wise linear model are shown in Figures 3.4(b) and (c), respectively.

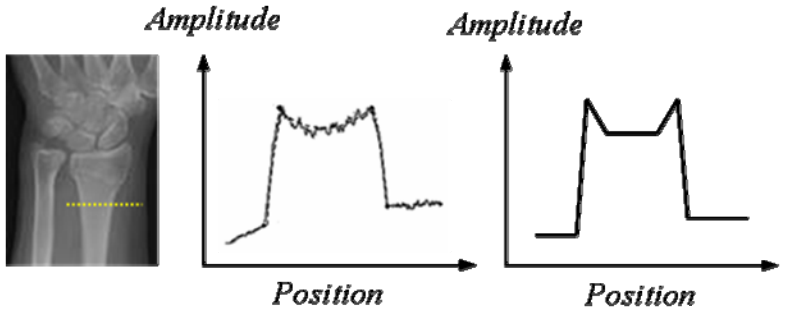

(a) (b) (c)

Figure 3.4 (a) radiograph of radius bone, (b) grey-level profile across the radius bone and (c) piece-wise linear model of the grey-level profile.

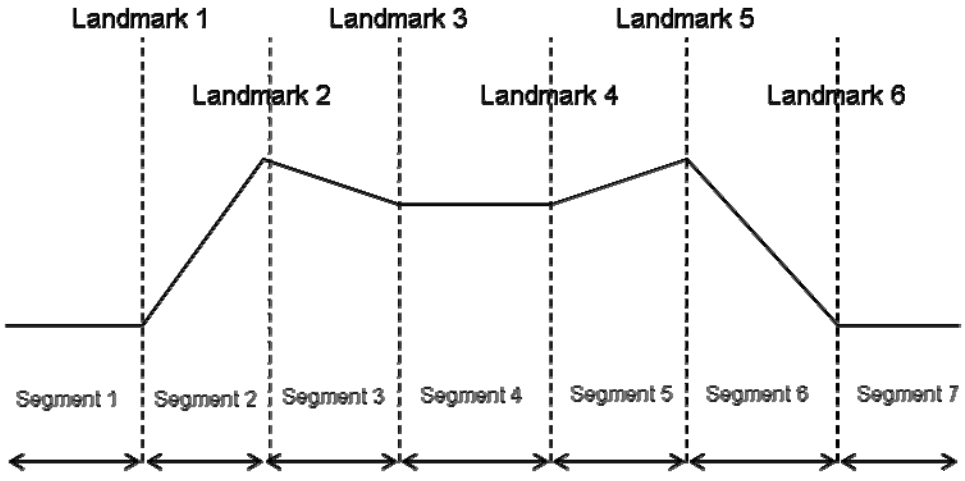

Figure 3.5 Seven-segment model with 6 landmarks to model a grey-level profile across the radius bone.

Figure 3.5 shows the piece-wise linear model to describe the profile across the radius bone. The model features 7 segments with 6 landmarks which were selected from edges, peaks and based points on the profiles.

Each segment was described by 4 parameters, the mean of the grey-level profile (μ), the standard deviation of the grey-level profile (σ) , the length of segment (l) and the slope of segment (η) as shown in the matrix below.

$$x_s = \begin{bmatrix} \mu_1 & \sigma_1 & l_1 & \eta_1 \\ \mu_2 & \sigma_2 & l_2 & \eta_2 \\ \mu_3 & \sigma_3 & l_3 & \eta_3 \\ \vdots & \vdots & \vdots & \vdots \\ \mu_n & \sigma_n & l_n & \eta_n \end{bmatrix}$$

Where x_s is the metric of parameters in a single profile

μ_i is the mean of grey-level profile in segment i

σ_i is the standard deviation of grey-level profile in segment i

l_i is the length of segment i

η_i is the slope of segment i

The matrix described a piece-wise linear model by segments in rows and parameters in columns. As the model has 7 segments; each segment is described by 4 parameters, therefore, the matrix x_s has a dimension of 7x4.

3.2.3 Cue generation

Cue generation is the process by which candidate breakpoints are generated in order to identify the segment divisions for building a model and for characterising an unseen grey-level profile. These breakpoints were generated using the detection of edges on the grey-level profile.

The maximum likelihood ratio was used to identify the edges. A pair of windows was moved along the path across the radius bone, as shown in Figure 3.6. The computation of likelihood

requires a statistically valid sample. The windows need to be small and to contain at least 16 samples (Pycock *et al.* 2000).

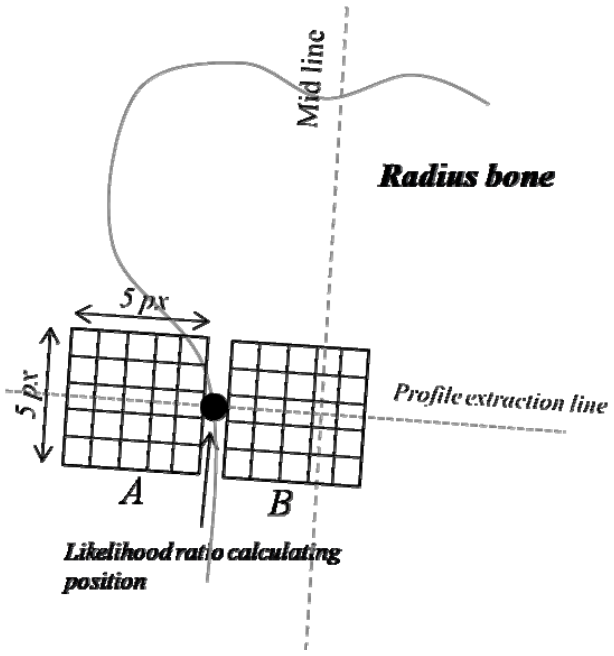

Figure 3.6 Two regions (A and B) were used to identify the bone edge using maximum likelihood ratio.

A pair of 5x5 windows was proposed as shown in Figure 3.6. The maximum likelihood ratio of the two populations, A and B is computed by

$$mlr = \frac{\sigma_{AB}^2}{\sigma_A \sigma_B}$$

Where σ is the standard deviation of the considering region

Peak detection was used to detect candidate breakpoints from the maximum likelihood ratio profile. The peaks were located using the peak detection with hysteresis algorithm, which has the potential to extract the weak boundaries between cortical and trabecular layers.

Figure 3.7 showed the pseudo code of the peak detection with hysteresis. The algorithm needed the peak height, *h*, and the peak width, *w* to be specified in order to locate the position of the peak. The peaks in a grey-level profile were located as points in the response with values greater (by *h*) than the values at points within the range of *w/2* pixels.

```
Let     p       be an array p representing a profile indexed from start to end and
        p[i]    be the value at position i in that profile.
        width   be width used to identify a peak
        peak    be the maximum value of profile
        Indexofpeak be the index at which the maximum peak is observed

For i=start to end-width
        If ( (p[i + width/2 -1] –p[i]) > height-1)
                If ( (p[i + width/2 -1] – p[i + width - 1]) > height -1)
                        If (p[I + width/2 -1] > peak)
                                Then    peak = p[i + width/2 -1]
                                        Indexofpeak = i + width/2 -1

For information the following is what was intended:
        m=0
        max =0

For i = start to end-width
        If ( (p[i + width/2 -1] – p[i]) > (height -1) )
                then    begpeak = TRUE
                        down = FALSE
                        start = i
                        posspeak = i + width/2 -1
                        then    for (k = posspeak to posspeak + width -1)
                                        If ( (p[posspeak] - p[k]) > height)
                                        then down = TRUE
        If ( (begpeak AND down) EQ TRUE)        then    if (p[posspeak] > max)
                                                         then   max = p[posspeak]
                                                                maxindex = posspeak
         If ( (begpeak EQ TRUE) AND (down EQ FALSE) ) then     peaklist[m]=posspeak
                                                                m = m + 1
                                                                begpeak = FALSE
```

Figure 3.7 The description of peak detection with hysteresis.

Large changes in grey-level, and strong edges, are readily detected because they produce large changes in maximum likelihood ratio. The weak boundaries between cortical and trabecular bone can also be detected because the edge produces a change of population between the two 5x5 pixel windows. A range of values for peak width and peak height was able to ensure that the required candidate breakpoints could be elected by the peak detection algorithm. Peak widths of 5, 10 and 15 pixels were used together with peak heights of 50 and 70 pixels.

The point at which the maximum likelihood ratio rises towards a peak can be detected with the aid of a simple transformation, which allows peak detection to be used. This transformation projects the response magnitude onto a line from the closest peak to the point and the base on the other side as shown as line AB in Figure 3.8.

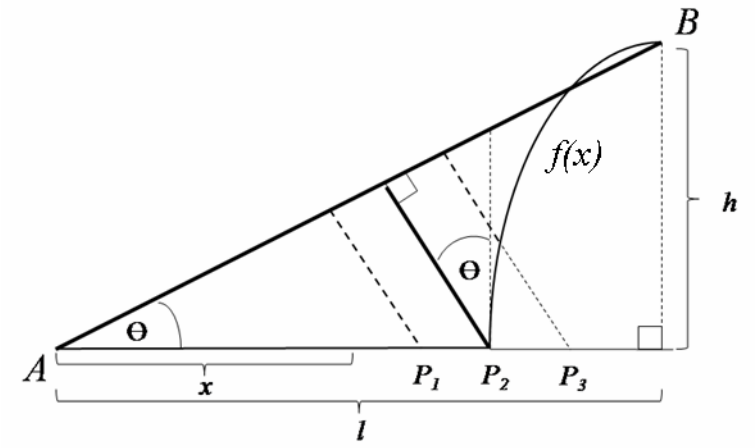

Figure 3.8 Transformation of point at which the response starts to rise to a peak with line AB.

For each point along the profile, a perpendicular line toward line AB is computed. The point of rising (P_2) is determined as the maximum response magnitude to line *AB*. Analytically this response magnitude is given by:

$$F_{pend}(x) = x\sin\theta - \frac{f(x)}{\cos\theta}$$

Where

$$\theta = \tan^{-1}\frac{h}{l}$$

θ is the angle of inclination of the base line for the projection

Only the candidate breakpoint that is most distant from the line AB is required to complete the cue generation.

3.2.4 Training method

A series of grey-level profiles across the radius bone were used in training a model. Landmarks were selected manually to create the best representation of segment divisions. These landmarks were used to calculate the piece-wise liner model of the grey-level profiles across the radius bone.

Training matrix (T) is:

$$T = \begin{bmatrix} (\mu_{1,1}, \sigma_{1,1}, l_{1,1}, \eta_{1,1}) & \cdots & (\mu_{1,N}, \sigma_{1,N}, l_{1,N}, \eta_{1,N}) \\ \vdots & \ddots & \vdots \\ (\mu_{n,1}, \sigma_{n,1}, l_{n,1}, \eta_{n,1}) & \cdots & (\mu_{n,N}, \sigma_{n,N}, l_{n,N}, \eta_{n,N}) \end{bmatrix}$$

n	is	the number of segments in a model
N	is	the number of profiles for training
i	is	1,2,3 ...n
j	is	1,2,3 ...N
$\mu_{i,j}$	is	the mean of grey-level amplitude in segment i of profile j
$\sigma_{i,j}$	is	the standard deviation of grey-level amplitude in segment i of profile j
$l_{i,j}$	is	the length of segment i of profile j
$\eta_{i,j}$	is	the slope of segment i of profile j

The mean of the parameter matrix ($\hat{\mu}$) is:

$$\hat{\mu} = \frac{1}{N}\begin{bmatrix} \sum_{j=1}^{N} T_{j,1}^{\mu} & \sum_{j=1}^{N} T_{j,1}^{\sigma} & \sum_{j=1}^{N} T_{j,1}^{l} & \sum_{j=1}^{N} T_{j,1}^{\eta} \\ \sum_{j=1}^{N} T_{j,2}^{\mu} & \sum_{j=1}^{N} T_{j,2}^{\sigma} & \sum_{j=1}^{N} T_{j,2}^{l} & \sum_{j=1}^{N} T_{j,2}^{\eta} \\ \sum_{j=1}^{N} T_{j,3}^{\mu} & \sum_{j=1}^{N} T_{j,3}^{\sigma} & \sum_{j=1}^{N} T_{j,3}^{l} & \sum_{j=1}^{N} T_{j,3}^{\eta} \\ \vdots & \vdots & \vdots & \vdots \\ \sum_{j=1}^{N} T_{j,n}^{\mu} & \sum_{j=1}^{N} T_{j,n}^{\sigma} & \sum_{j=1}^{N} T_{j,n}^{l} & \sum_{j=1}^{N} T_{j,n}^{\eta} \end{bmatrix}$$

$T^{t}_{j,i}$ is the value in column j row i for parameter t, $t = (\mu, \sigma, l, \eta)$

The variance of parameter (V) is

$$V = \frac{1}{N}\begin{bmatrix} \sum_{j=1}^{N}\left(T_{j,1}^{\mu} - \hat{\mu}_{1,1}\right)^2 & \sum_{j=1}^{N}\left(T_{j,1}^{\sigma} - \hat{\mu}_{1,1}\right)^2 & \sum_{j=1}^{N}\left(T_{j,1}^{l} - \hat{\mu}_{1,1}\right)^2 & \sum_{j=1}^{N}\left(T_{j,1}^{\eta} - \hat{\mu}_{1,1}\right)^2 \\ \sum_{j=1}^{N}\left(T_{j,2}^{\mu} - \hat{\mu}_{2,1}\right)^2 & \sum_{j=1}^{N}\left(T_{j,2}^{\sigma} - \hat{\mu}_{2,1}\right)^2 & \sum_{j=1}^{N}\left(T_{j,2}^{l} - \hat{\mu}_{2,1}\right)^2 & \sum_{j=1}^{N}\left(T_{j,2}^{\eta} - \hat{\mu}_{2,1}\right)^2 \\ \sum_{j=1}^{N}\left(T_{j,3}^{\mu} - \hat{\mu}_{3,1}\right)^2 & \sum_{j=1}^{N}\left(T_{j,3}^{\sigma} - \hat{\mu}_{3,1}\right)^2 & \sum_{j=1}^{N}\left(T_{j,3}^{l} - \hat{\mu}_{3,1}\right)^2 & \sum_{j=1}^{N}\left(T_{j,3}^{\eta} - \hat{\mu}_{3,1}\right)^2 \\ \vdots & \vdots & \vdots & \vdots \\ \sum_{j=1}^{N}\left(T_{j,n}^{\mu} - \hat{\mu}_{n,1}\right)^2 & \sum_{j=1}^{N}\left(T_{j,n}^{\sigma} - \hat{\mu}_{n,1}\right)^2 & \sum_{j=1}^{N}\left(T_{j,n}^{l} - \hat{\mu}_{n,1}\right)^2 & \sum_{j=1}^{N}\left(T_{j,n}^{\eta} - \hat{\mu}_{n,1}\right)^2 \end{bmatrix}$$

Thus, the standard deviation of the parameter matrix ($\hat{\sigma}$) is

$$\hat{\sigma} = \begin{bmatrix} \sqrt{V_{1,1}} & \cdots & \sqrt{V_{1,k}} \\ \vdots & \ddots & \vdots \\ \sqrt{V_{n,1}} & \cdots & \sqrt{V_{n,k}} \end{bmatrix}$$

k is the number of parameters used (the number of columns in x_s)

This project used 4 types of parameters (k = 4) based on the 7-segment model (n = 7) to train with 25 samples (N = 25). The influence of gender could be considered by training male and female samples separately. The matrices T, $\hat{\mu}$ and $\hat{\sigma}$ are used to create a flexible model used to guide the process of interpretation.

3.2.5 Interpretation Process

The methods to match unseen profiles to the model are described. The model parameters were used to the compare the closeness between the model and the profile. The model parameters are weighted with respect to one another using mean ($\hat{\mu}$) and standard deviation ($\hat{\sigma}$) of the parameters.

The normalised parameter matrix ($\hat{x}_s^{'}$) is

$$\hat{x}_s^{'} = \begin{bmatrix} \frac{x_{s\,1,1} - \hat{\mu}_{1,1}}{\hat{\sigma}_{1,1}} & \cdots & \frac{x_{s\,1,k} - \hat{\mu}_{1,k}}{\hat{\sigma}_{1,k}} \\ \vdots & \ddots & \vdots \\ \frac{x_{s\,n,1} - \hat{\mu}_{n,1}}{\hat{\sigma}_{n,1}} & \cdots & \frac{x_{s\,n,k} - \hat{\mu}_{n,k}}{\hat{\sigma}_{n,k}} \end{bmatrix}$$

$\hat{x}_s^{'}$ is the matrix of normalised parameters with n segments in (rows) and k parameters (columns).

An interpretation of various parameters requires an appropriate weight. The parameters weight was defined by population variance for each parameter. To compare between a model and profile, standard deviation was used to normalize the matching and weight model parameters according to their degree of variation.

For example; $x_{s1,1}$ is the mean amplitude of segment 1 of the unseen profile, $\hat{\mu}_{1,1}$ is the mean amplitude of segment 1 of the model and $\hat{\sigma}_{1,1}$ is the standard deviation of amplitude of segment 1 of the model. The column of the matrix represents the parameters; mean of amplitude, standard deviation of amplitude, segment slope and segment length, respectively for columns 1 to 4.

The normalised parameter matrix was a measure of the similarity between the profile and the model. If the parameter of the profile is close to the model, the similarity measurement will be close to zero.

Table 3-1 shows the model parameters of the bone profile model by segment. For instance; segment 1 is described only by the standard deviation of the profile amplitude. Segment 2 is described by the segment length, the standard deviation of the profile amplitude, the amplitude and the segment slope.

Mask A is used to indicate which parameters are used. This simplifies changes to the model representation; 0 is used to signify not-selected and a 1 to signify selected as shown in the following matrix. The columns represent the parameter, in order μ, σ, l and η. The rows represent the segments.

Table 3-1 Parameters of the model.

Segment	**Parameter**
1	Standard deviation of segment amplitude
2	Mean segment length Standard deviation of segment amplitude Segment slope
3	Mean length Standard deviation of segment amplitude
4	No important parameters
5	Mean length Standard deviation of segment amplitude
6	Mean length Standard deviation of segment amplitude Segment slope
7	Standard deviation of segment amplitude

$$A = \begin{array}{c} \begin{matrix} \mu & \sigma & l & \eta \end{matrix} \\ \begin{bmatrix} 0 & 1 & 0 & 0 \\ 0 & 1 & 1 & 1 \\ 0 & 1 & 1 & 0 \\ 0 & 0 & 0 & 0 \\ 0 & 1 & 1 & 0 \\ 0 & 1 & 1 & 1 \\ 0 & 1 & 0 & 0 \end{bmatrix} \end{array} \begin{array}{l} Segment1 \\ Segment2 \\ . \\ . \\ . \\ . \\ segment7 \end{array}$$

Mask A is used to calculate the difference between a profile and a model (P_{match}), computed as the sum of the squared difference, i.e.:

$$P_{match} = \sum_{j=1}^{k} \sum_{i=1}^{n} A_{ji} \left(\hat{x}_s{}'_{ji} \right)^2$$

A small value of P_{match} indicates that the unseen profile is a close match to the model. The search process uses dynamic programming to find the best match for each segment in turn, from the remaining segments in the profile as described in Figure 3.9. Segments 1 to k are selected and matched one-by-one to segments in the model. Segments are merged as appropriate to obtain the best match.

1. For each segment in a model
   1.1 For each candidate breakpoint in a profile
      1.1.1 Compute matching criteria of candidate current segment with a model
      1.1.2 If matching criteria at segment k+1 > segment k
            Merge candidate segment k and k+1
         else (when the best match found)
            Stop merging
         Progress to the next segment

Figure 3.9 Description of search strategy.

The interpretation was used to construct the model from unseen profiles in order to measure the bone thickness. 43 male samples and 23 female samples were used to interpret the results and measure the bone thickness

3.3 Implementations

3.3.1 A simulation of a grey-level profile from an X-ray of the radius

A synthetic grey-level profile was created by a simulation of the X-ray radiographic process in order to help to:

- define landmarks on the grey-level profile
- design a suitable model for the grey-level profile
- locate the position of internal and external radius on the grey-level profile

Another purpose of this experiment was to investigate the shape of the maximum likelihood ratio which responds to the bone profile. This investigation helps to:

- show that mlr operator can be used in the synthetic profile
- consider positions on mlr profile that respond to the feature points of the synthetic profile

A narrow beam of mono-energetic photons with incident intensity I_o, penetrating a layer of material with mass thickness x and attenuation coefficient ρ, emerges with intensity I given by the exponential attenuation law:

$$I = I_0 e^{-\rho x} \tag{3.1}$$

Table 3-2 showed the attenuation coefficients for each component of the forearm. The tissue and the trabecular layer have a lower coefficient than the cortical bone, which provide a lower attenuation level of the X-ray.

Table 3-2 X-ray mass attenuation coefficient of materials at an initial energy of 1MeV

Material	**Coefficient (ρ)** (g/cm^3)
Tissue	0.9
Cortical bone	2.0
Trabecular bone	1.4

Figure 4.1 (b) shows the simplified cross-section structure of the radius bone. The X-ray attenuation equation was used to simulate a grey-level profile across the radius in the scale of 0-255.

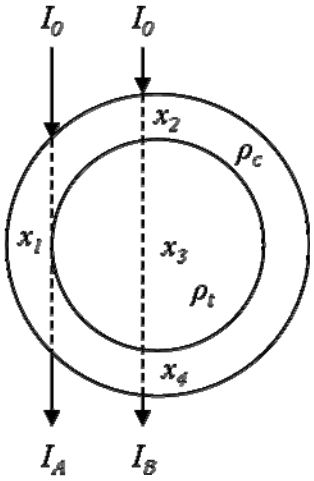

Figure 3.10 An illustration of X-ray energy at position A and B of the radius bone

X-ray energy at position A is

$$I_A = I_0 e^{-\rho_c x_1}$$

Where ρ_c is attenuation coefficient of cortical layer; x_1 is shown in Figure 3.10.

X-ray energy at position B is

$$I_B = I_0 e^{-\rho_c (x_2 + x_4) - \rho_t x_3}$$

Where ρ_t is attenuation coefficient of trabecular layer; x_2, x_3 and x_4 are shown in Figure 3.10.

Computation of the maximum likelihood ratio involved the standard deviation of small samples from the image. For the simulated grey-level profile, in the absence of detection noise the standard deviation was sometimes zero, or close to zero. Dividing by zero or a

value close to zero can result in over estimation of maximum likelihood ratio. To avoid exceeding such errors a very small value of Gaussian distributed noise was added to the profile, equivalent to a SNR = 46dB.

A program to generate of the X-ray attenuation was developed as shown in Figure 3.11. The bone dimensions and X-ray attenuation coefficients are displayed but cannot be edited. The thickness (Δr) of 20 pixels, and radius (r_o) of 150 pixels were set in this experiment to simulate the mean dimension of the radius bone. The X-ray energy at 1 MeV was initiated to run the simulation to observe the result.

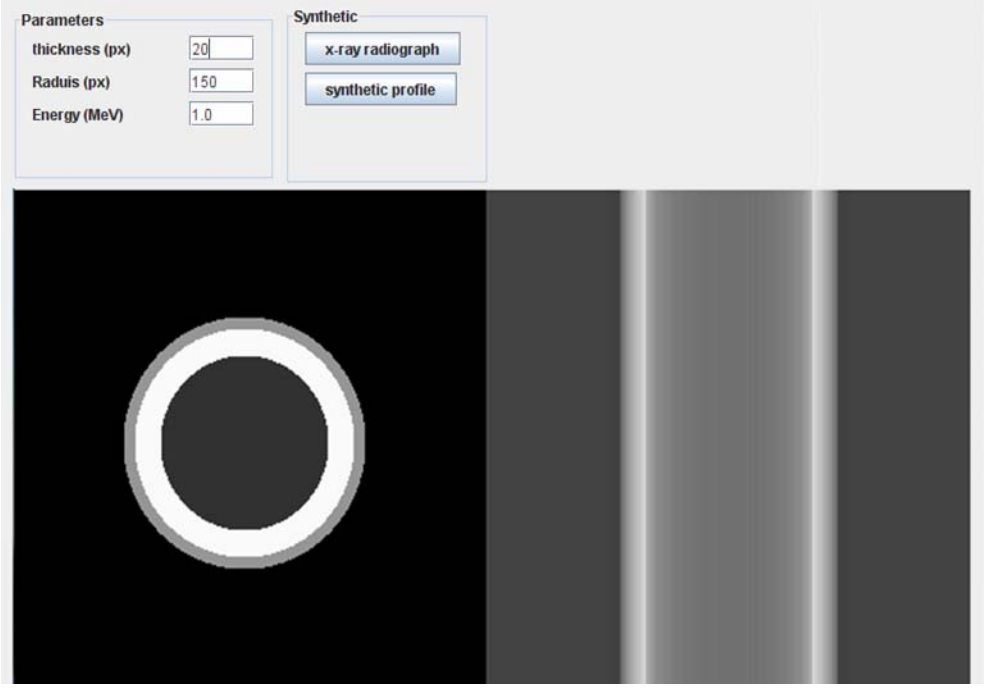

Figure 3.11 The interface for the program used to create the synthetic radiograph and grey-level profile.

3.3.2 Training and interpretation of the grey-level profile

This experiment performed the training and the interpretation process in order to:

- observe the variations of the model parameters

- use the model to interpret unseen profiles and measure the bone thickness
- calculate the margin of error when measuring the bone thickness.

Six landmarks were selected manually from candidates, generated as described in section 3.2.3, in order to train a model as in section 3.2.4 on 25 instances of grey-level profiles. Landmarks were used to divide the grey-level profile into several segments and calculate segment parameters. The parameters and their variations were observed by plotting graphs of their mean and standard deviation shown by parameter type, segment and gender.

The users select/deselect breakpoints to form a model by clicking inside the relevant box of breakpoints. When the breakpoints have been selected, the user may request to compute the model. Figure 3.12 shows the grey-level profile used in training. The dots showed the position of candidate breakpoints. The filled dots are the breakpoints which were selected as the landmarks of the model.

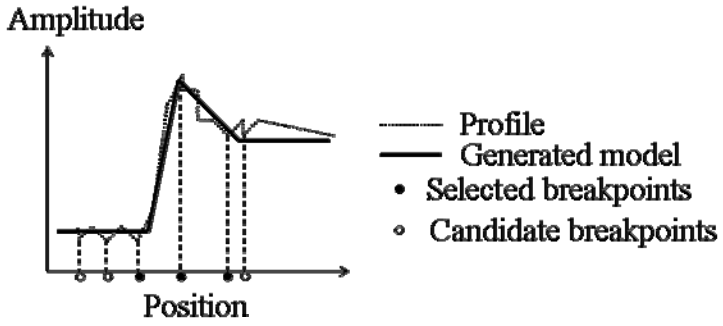

Figure 3.12 Candidate breakpoint and selected landmarks identified in the training phase.

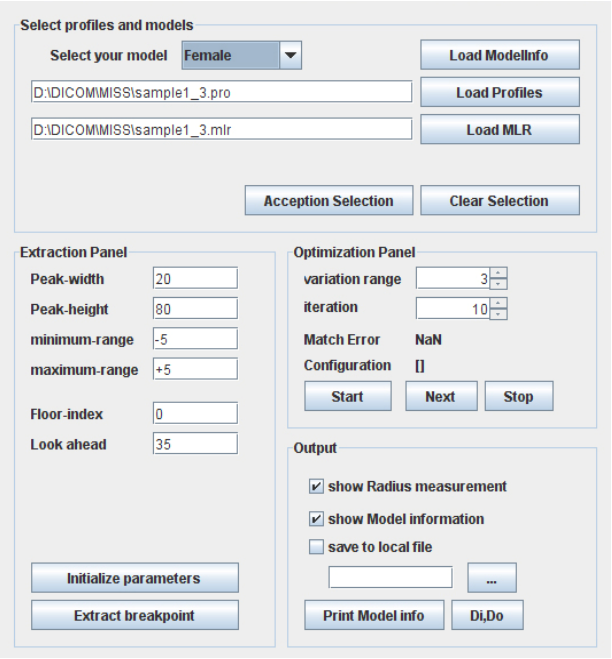

Figure 3.13 the interpretation dialog

Figure 3.13 shows the interpretation dialog which was used to control the interpretation of an unseen grey-level profile. Firstly, users have to select the model and the gender of the subjects. The user may also set parameters in the interpretation process, including Peak-width, Peak-height, range minimum and maximum. Changing these parameters will alter the number of breakpoints generated. The floor index and look-ahead parameters are the parameters for the floor detection algorithm. The user can set parameters for merging segments to control the dynamic programme search using the optimization. This panel showed the error between the profile and the model with the configuration of breakpoints. Users can run dynamic programming matching with one-long-step or step-by-step in order to observe the segment matching and stop the interpretation process whenever they wish to observe the current configuration of breakpoints. The output panel is used to select the information to be output, such as, the radius (r_i and r_o), model data and to be able to save any of these outputs as a text file.

The matched model provides an estimate of bone thickness. A basic evaluation of the interpretation was performed by comparing automated and manual estimates of bone thickness for 36 male and 34 female samples as described in section 3.2.5. The difference of the inner and outer bone radius between the manual and automated estimates of bone thickness is shown in Figure 3.14, as Δr_i and Δr_o respectively.

Δr_i is the difference between the manual and automated of inner radius.

Δr_o is the difference between the manually and automated of outer radius.

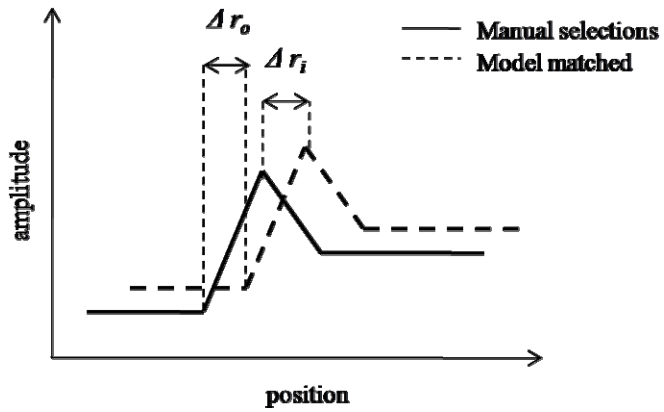

Figure 3.14 Definition of radius error.

The error was computed as a percentage of the corresponding radius.

$$\% \text{ error of } \Delta r_i = \frac{\Delta r_i}{\text{diameter of radius bone}}$$

$$\% \text{ error of } \Delta r_o = \frac{\Delta r_o}{\text{diameter of radius bone}}$$

3.3.3 Risk of fracture evaluation

It was hypothesised that there is a strong dependence between bone thickness and the risk of a fracture. Whilst it is clear that errors in estimating the thickness of cortical bone will give rise to errors in estimating the risk of fracture. It is not clear how critical such errors will be

without knowing how the computed parameters differ for those at risk of a fracture and those who are not.

The objectives of this experiment were to:

- assess the risk of fracture of the samples in the project and to identify those with high risk of fracture
- evaluate the criteria used to separate between the high risk and low risk subjects.
- calculate student's T-test between the high risk and low risk subjects

It is also difficult to formulate a test which requires knowledge of a fracture in order to assess the reliability of the risk of fracture estimation. The time constraints on this project and the availability of the data mean that a follow up study is not possible as part of the present evaluation. Instead the X-ray images for those who, following a trauma, have and have not suffered a Colles' fracture will be analysed. Radiographs with fracture subjects and non fracture subjects were matched with a model and measured the thickness of the radius bone. 17 cases of fractured samples (9 male and 8 female) and 66 cases of non-fractured samples (43 male and 23 female) were available for study.

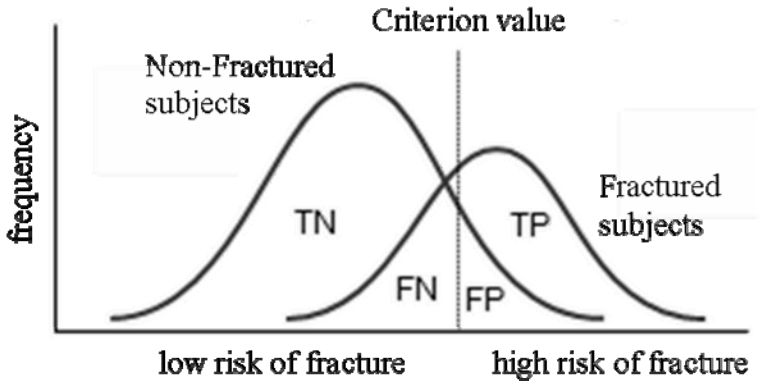

Figure 3.15 Fractured and non-fracture subjects and the criterion value to detect high risk of fracture subjects.

It was assumed that the distributions of fractured and non-fractured subject was Gaussian, as illustrated in Figure 3.15. We used the criterion value in Figure 3.15 to separate between those who had previously experienced a fracture and those who had not.

The criteria proposed in this experiment are:

μ_{nf}	the mean of the risk of fracture of non-fracture subjects
μ_f	the mean of the risk of fracture of fracture subjects
MEAN	the mean of the risk of fracture of all subjects
$\pm n\ SD$	the standard deviation of the risk of fracture, n = 1,2 and 3
±5%	±5% of the MEAN.

The subjects with risk estimation less than the criterion value can be detected to have a low risk of fracture, those with more to have a high risk of fracture. Criterion value is based on the average values and standard deviation of risk estimation.

The evaluation of criteria can be assessed by the following parameters:

False negative (FN):	the number of fracture subjects which were detected to have a low risk of fracture
False positive (FP):	the number of non-fracture subjects which were detected to have a high risk of fracture
True negative (TN):	the number of non-fracture subjects which were detected to have a low risk of fracture
True positive (TP):	the number of fracture subjects which were detected to have a high risk of fracture

Student's T-test was used to calculate the risk estimation difference between fractured and non-fractured samples. Unequal sample sizes and unequal variance in populations were assumed as the distribution shown in Figure 3.15. Therefore, the t-test of the two groups (high and low risk) was calculated by

$$t = \frac{\mu_f - \mu_{nf}}{\sigma_{\mu_f - \mu_{nf}}}; \sigma_{\mu_f - \mu_{nf}} = \sqrt{\frac{\sigma_f^2}{N_f} + \frac{\sigma_{nf}^2}{N_{nf}}}$$

μ_f	the mean of risk estimation of fractured samples.
μ_{nf}	the mean of risk estimation of non-fractured samples.
σ^2_f	the variance of risk estimation of fractured samples.
σ^2_{nf}	the variance of risk estimation of non-fractured samples.
N_f	the number of fractured samples.
N_{nf}	the number of non-fractured samples.

The degree of freedom was computed by

$$D.F. = \frac{\left(\frac{\sigma_f^2}{N_f} + \frac{\sigma_{nf}^2}{N_{nf}}\right)^2}{\frac{\left(\frac{\sigma_f^2}{N_f}\right)^2}{N_f - 1} + \frac{\left(\frac{\sigma_{nf}^2}{N_{nf}}\right)^2}{N_{nf} - 1}}$$

4 RESULTS

A synthetic profile and maximum likelihood ratio was shown in order to observe the shape of the bone profile. The parameters of the bone profile model were observed by training a series of grey-level profiles across the radius bone. The model interpretation and the accuracy of measuring the internal and external radius were assessed by comparing between automated and manual estimations. Finally, the risk of fracture was evaluated by showing a scatter graph between fractured and non-fractured samples.

4.1 Synthesis of the bone profile

Figure 4.1 (a) shows the synthetic profile across a radius bone (solid line). The results simulated an X-ray with the outer radius of 65 pixels and the internal radius of 50 pixels.

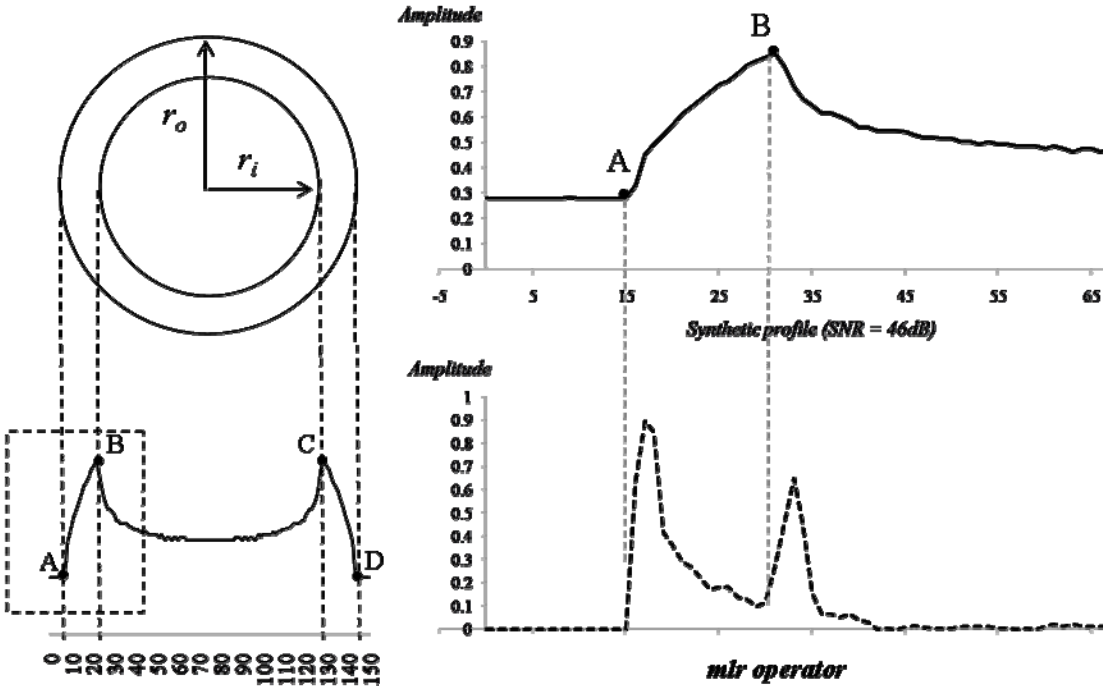

(a) (b)

Figure 4.1 (a) landmarks of the inner and outer edge of the simulated cortical bone and (b) simulated grey-level profile (top) and mlr response.

The amplitude at the beginning of the profile is low and steady and then it is rapidly raised. In the middle of the profile the amplitude seems steady again but the mean of grey-level amplitude is higher than the mean at the beginning. The mean of the grey-level amplitude at the beginning represents the attenuation of the soft tissue layer. In the middle section the mean represents the attenuation of the central bone core in the simulation.

The outer edge of the bone fits the point where the simulated grey-level profile begins to rise, corresponding to points A and D, and the peak of the grey-level profile fits the inner edge of

the cortical bone, corresponding to points B and C. These are the landmarks with which the internal and external radius can be computed.

Figure 4.1 (b) shows the mlr response for the simulated grey-level of the synthetic profile. Maximum likelihood ratio of the synthetic profile (with SNR=46dB), is shown in the profile as a dotted rectangular box in Figure 4.1 (a). Figure 4.1 (b) shows that there are two peaks in the mlr profile.

The first peak of the mlr profile corresponds to the position of the outer wall of the cortical bone. The second peak corresponds to the position within the bone where attenuation seems to be steady. The first peak is higher and wider than the second. Position A, to measure the outer radius, responds to the dip of mlr operator aligns with the first peak. Position B to measure the inner radius responds to the local minimum of mlr profile.

4.2 Bone profile variations

The following bar graphs shows the results of training. Each bar graph shows the mean magnitude of a model parameter with error bars, representing the standard deviation of the model parameter. Male and female results are shown in Figure 4.2 and 4.3 respectively.

Figure 4.2 (a) and 4.3 (b) shows the segment length of the profile. The fourth segment seems to be the longest and has a large standard deviation. The segment amplitude is very variable as shown in Figures 4.2 (b) and 4.3 (b). Figures 4.2 (c) and 4.3 (c) shows the standard deviation of the segment amplitude. These standard deviations are very large in the second and the fourth segment and small in other cases. Figures 4.2 (d) and 4.3 (d) shows the segment slope which becomes positive when it is rising to the peaks and negative when it goes in the opposite direction. The slope magnitude of the second and the sixth segment is high whilst the slope magnitude of the third and the fifth segments is small.

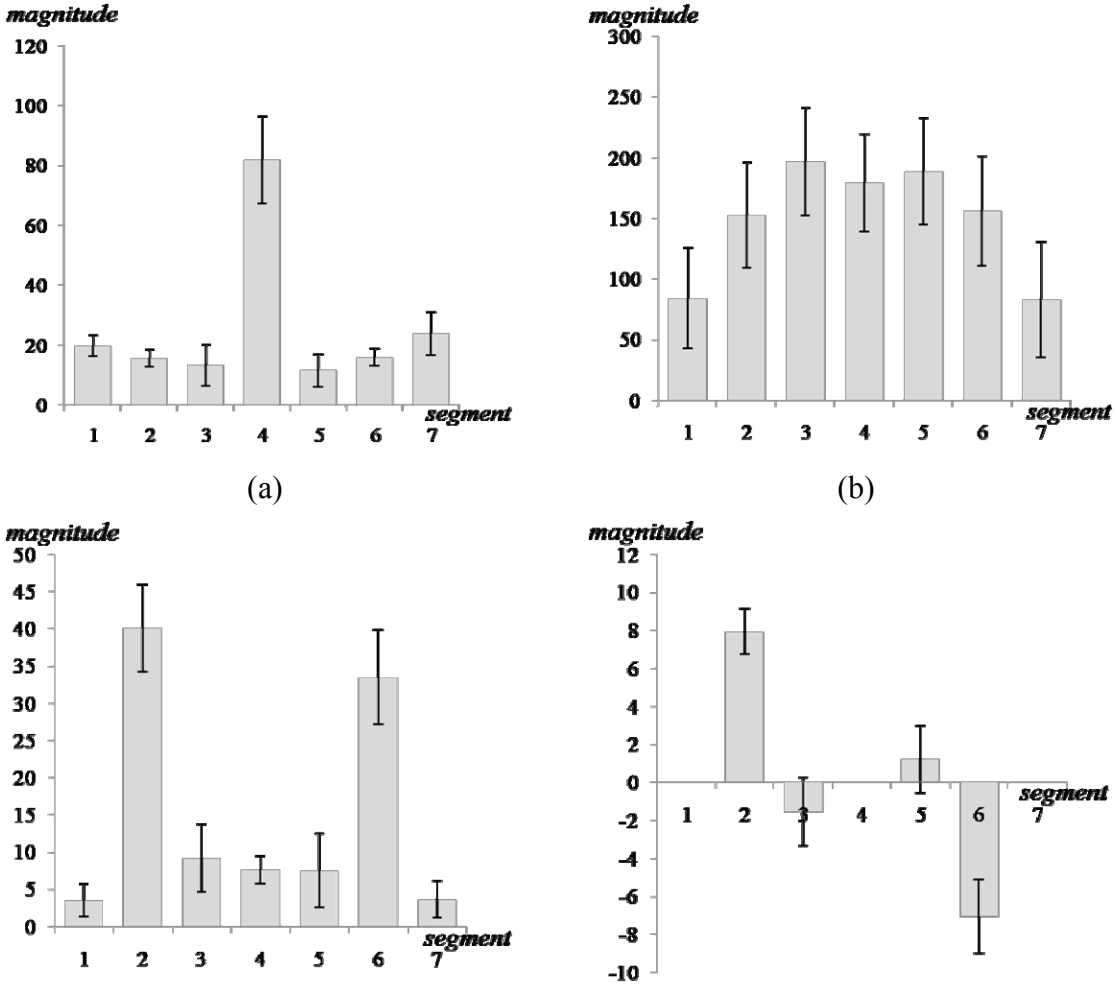

Figure 4.2 The training results of grey-level profiles of the male radius bones; the bars are the average of each parameter over those indicated segment and the error bars are the standard deviation of the relevant parameters. The parameters represented are: (a) segment length, (b) segment amplitude, (c) standard deviation of segment amplitude and (d) segment slope.

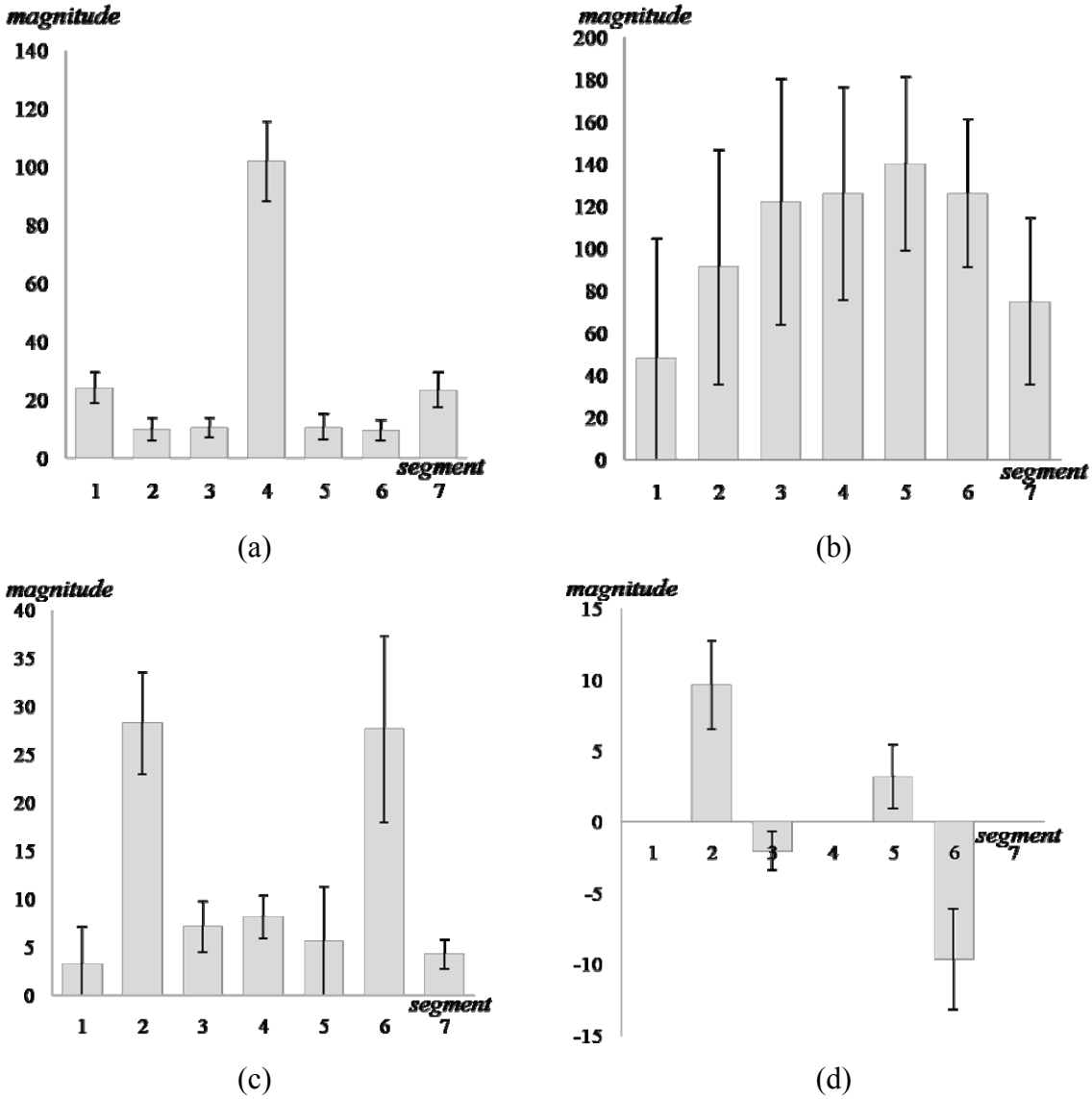

Figure 4.3 The training results of grey-level profiles of the female radius bones; the bars are the average of each parameter over the indicated segment and the error bars are the standard deviation of the relevant parameters. The parameters represented are: (a) segment length, (b) segment amplitude, (c) standard deviation of segment amplitude and (d) segment slope.

4.3 The error of bone thickness measurement

Figure 4.4 (a) and 4.4 (b) shows the percentage error of bone thickness measurement of male and female subjects respectively. The graphs illustrate the percentage of error in the x-axis against the number of samples (frequency) in the y-axis. A negative value of error means the measured radius is less than actual value, whilst, a positive value of error means the measured

radius is overestimated. The histogram shows most of the samples produce a small error, less than ±2%. Only 2 samples produced a large error of ±5%.

The long dashed line represents the internal radius error and short dashed line represents the external. The results show that the variation of error in the internal radius is less than that of the external. Table 4-1 shows that the standard deviation of internal radius measurement is smaller than that of external radius. The standard deviation of errors also showed that the radius measurement in female subjects shows smaller variation than that in male subjects.

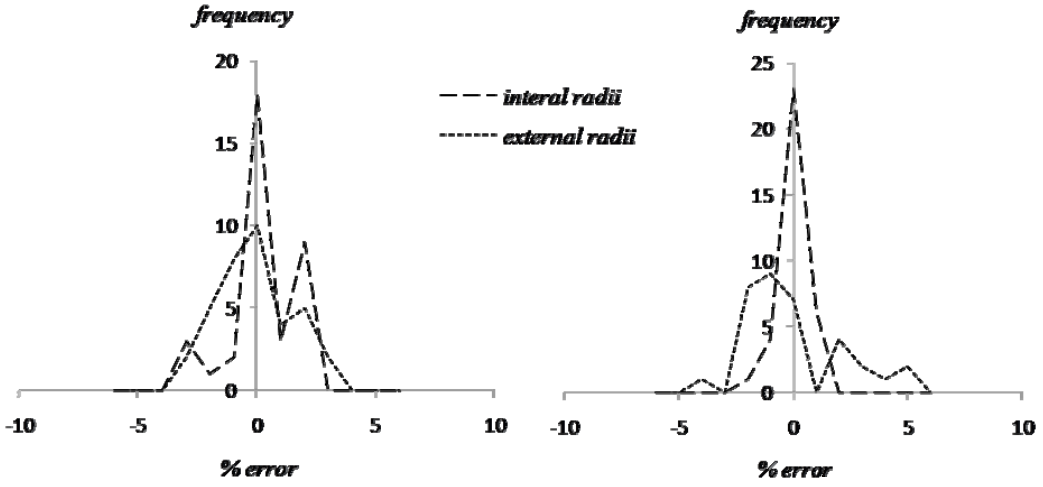

(a) (b)

Figure 4.4 Histograms of percentage of error in the internal and external radius measures (a) male samples (b) female samples

Table 4-1 Standard deviation of radius error by gender

	Samples	**SD of $\%\Delta r_i$**	**SD of $\%\Delta r_o$**
Male	36	1.1	1.6
Female	38	0.7	1.2

Table 4-2 Margin of error in the bone thickness measurement

	Margin of error with 90% confidence		**Margin of error with 95% confidence**		**Margin of error with 99% confidence**	
	$\%\Delta r_i$	**$\%\Delta r_o$**	**$\%\Delta r_i$**	**$\%\Delta r_o$**	**$\%\Delta r_i$**	**$\%\Delta r_o$**
Male	0.3	0.4	0.4	0.5	0.5	0.7
Female	0.2	0.3	0.2	0.4	0.3	0.5

Table 4-2 shows the small margin of error, computed by the standard deviation of radius error, with 90%, 95% and 99% confidence in order to show the reliability of the bone profile model interpretation. The margin of error is less than 1% in both male and female subjects - male subjects have 0.1 – 0.2 % higher than the female.

4.4 The risk of fracture estimation

The risk of fracture for subjects with a fracture (shown as ×) and without (shown as +) were assessed. The risk of fracture estimates were plotted on a log scale as shown in Figure 4.5. The domain unit of risk of fracture is within 10^{-2} to 10^{-5}. The means of the risk of fracture of non-fractured subjects (μ_{nf}) and fracture subjects (μ_f) were shown by dashed lines in Figure 4.5.

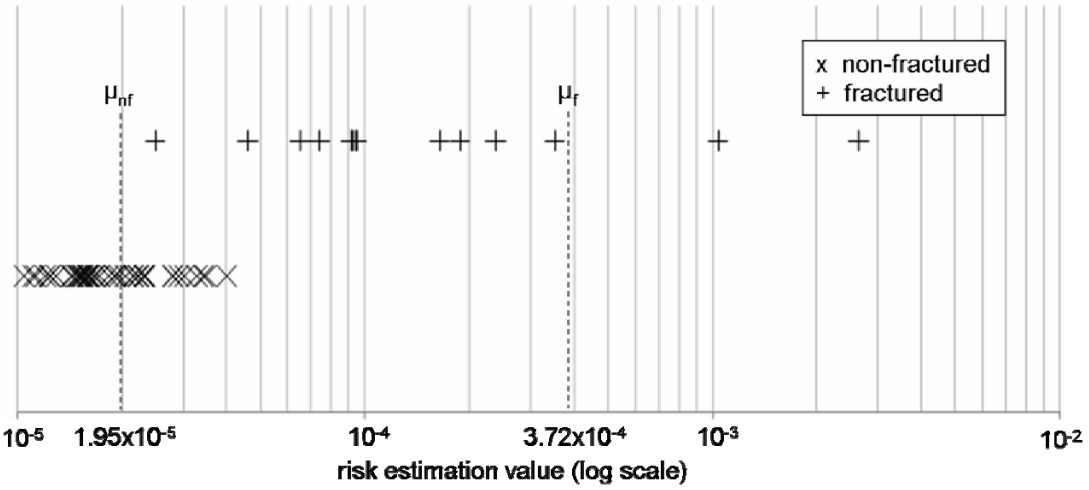

Figure 4.5 Log scale of risk estimation for subjects having experienced and not experienced a fracture.

Non-fracture subjects showed a low variation of estimated risk while fracture subjects showed a wide-range of variation in the risk. Figure 4.5 also shows evidence of a bimodal split between the values from those who have had a fracture and those who have had not.

Figure 4.6 is a scatter diagram representing the risk of fracture. The x-axis represents the external radius in the domain 0-4 mm and the y-axis represents bone wall thickness in the domain of 0-18 mm.

Values to the right represent a low risk of fracture and those to the left a high risk of fracture. Curves in Figure 4.6 represent the possible boundaries for determining those with a high risk for a fracture. The lines are the population mean risk of fracture estimates and contours at ± 1 SD, ± 2SD and ± 5% of the population mean of risk of fracture estimates which represents the influence of the uncertainty in the estimation of the risk.

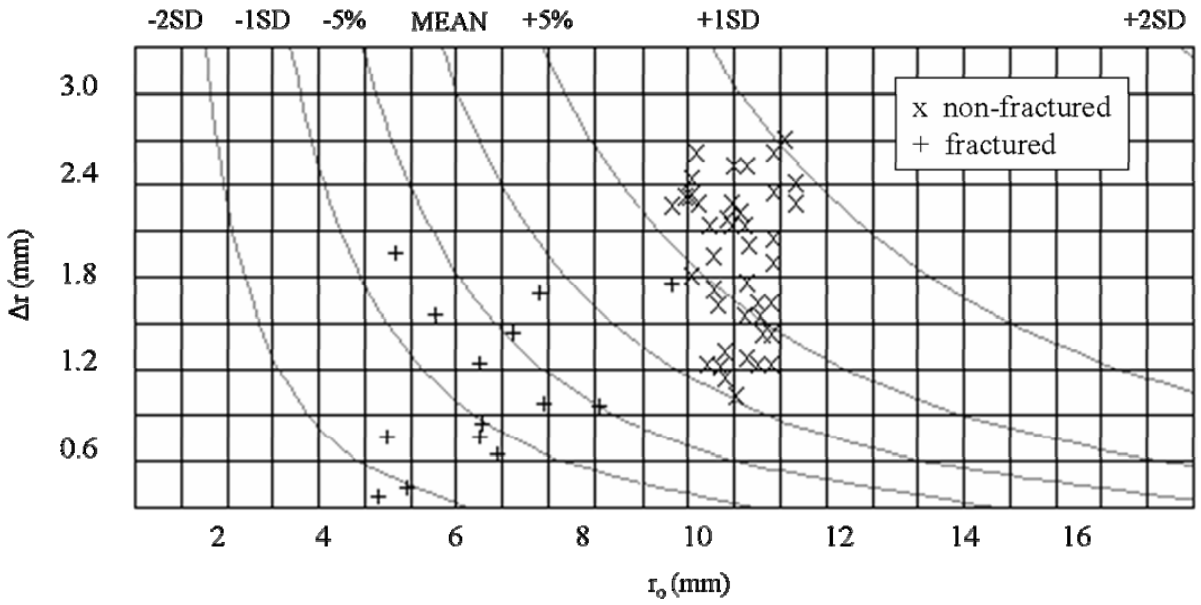

Figure 4.6 A scatter graph of subjects having had and not had a fracture in the domain of the external radius (y-axis) and the cortical bone thickness (x-axis).

The possible boundaries separate the samples into two groups (high and low risk of fracture). Non-fractured subjects should be detected as the low risk of fracture; whilst, fracture subject should be detected as high. We counted the number of samples which were on the wrong side of the boundaries to evaluate the number of false negative (fractured subjects detected as low risk) and the number of false positive (non-fractured subjects detected as high risk).

Figure 4.7 shows the percentage of false negatives on the y-axis and false positives on the x-axis. When the boundary was at +5%, it showed a 20% false negative and 0% false positive. The most compromised boundary is the MEAN shows 0% of false negative and less than 5% (one case) of false positive.

Table 4-3 shows the number of samples, mean and standard deviation of risk estimation of fractured and non-fracture subjects used to calculate student's t-test which showed a confidence of 92% in population difference. The data is unequal sample sizes and unequal variance in populations as the number of samples and standard deviation shown in Table 4-3.

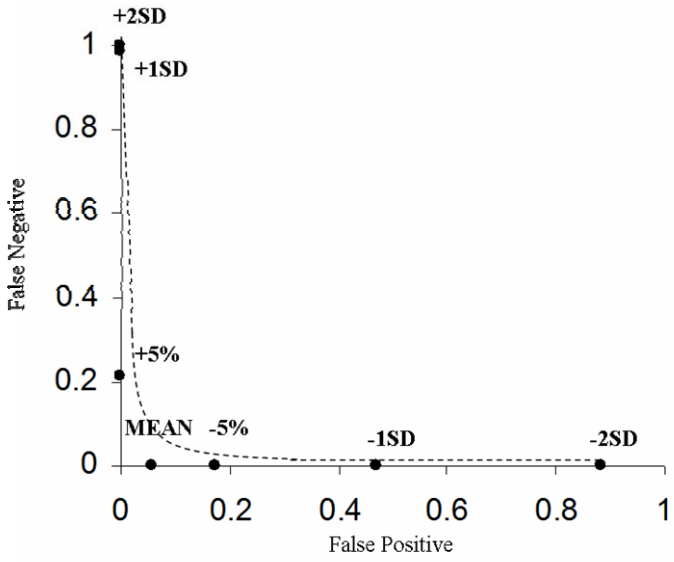

Figure 4.7 False negative and false positive error rates of the risk estimation.

Table 4-3 Number, mean and standard deviation of risk estimation of fractured and non-fracture subjects.

	Samples	**Mean of risk estimation**	**SD of risk estimation**
Fracture subject	17	3.72×10^{-4}	7.03×10^{-4}
Non-fracture subject	66	1.95×10^{-5}	7.14×10^{-6}

5 DISCUSSIONS

5.1 The shape of the synthetic bone profile and mlr response

The synthetic profile showed the locations corresponding to the boundary in the bone profile model. The outer edge of the bone appears to correspond to the point where the simulated grey-level profile has risen a little above the tissue level. It was surprising that the peak in the synthetic bone profile corresponded to the inner edge of the cortical bone.

Maximum likelihood ratio responded to ramp edges of the synthetic profile. Figure 5.1 shows that the grey-level population in a pair of windows differ most at the point where the ramp edge begins to rise (between A and B).

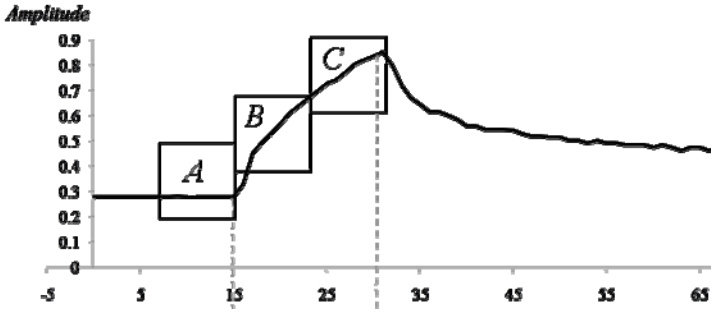

Figure 5.1 Regions A, B and C representing window on synthetic bone profile

A local minimum of mlr operator responded to the peak of the bone profile. At this position (beyond C), the slope of the magnitude is changing from positive to negative but the standard deviation on the two sides of the peak are almost the same giving a minimal of mlr response.

The inner and outer radius of the radius bone can be identified from a grey-level profile across the radius bone. The study of maximum likelihood ratio of synthetic profile helps to define a suitable model and also to design a model interpretation strategy.

5.2 Model parameters

The results showed that there are potential parameters that can be used as signatures of a bone profile model as discussed below.

Segments 1 and 7: These segments are the beginning and the end of the attenuation of the bone profile. These segments were expected to have a low degree of amplitude variation because it showed the attenuation of the tissue layer and a high degree of segment length variation because it is a one-end opened segment. Therefore, these parameters were not suitable for use as signature parameters. The standard deviation of the segment amplitude was the only parameter used in these segments.

Segments 2 and 6: These segments revealed the profile shape with 2 peaks. The standard deviation of the profile amplitude is relatively big compared to the other segments because segments 2 and 6 covered a range of changing grey-level amplitude as X-ray penetrates the tissue through the bone. Clearly the amplitude is not a suitable parameter with which to model this segment, but the distinctively large standard deviation on these segments can be useful. The standard deviation of grey-level amplitude, segment slope and length were the model parameters used.

Segments 3 and 5: These segments covered the transition from cortical to trabecular bone and therefore the grey-level profile is likely to vary from one case to another and it is difficult to identify suitable model parameters. However, the standard deviation of segment-amplitude and segment length has a low degree of variation were therefore selected as model parameters.

Segment 4: All the parameters of this segment have a high degree of variation and it is difficult to identify any suitable model parameters. This is attributed to the variable nature of

the trabecular bone that forms a significant part of the X-ray path length for this segment. Therefore, no appropriate model parameters could be identified for this segment.

Slope and standard deviation have the potential to be feature parameters of the model because of their low degree of variation. Segment length is useful to limit the boundary of interpretation in segment 2, 3, 5 and 6.

The results of training between male and female samples did not show a difference, therefore, the models can be similar and replaceable between the two. However, the variation of segment amplitude of female subjects is little higher than that of male.

Since the proposed model is a common structure of the bone, this training result might help represent other bones in the body. However, the model parameters need to be tuned.

5.3 Evaluations of the model interpretation

The grey-level profiles from the X-ray images of the forearm were successfully matched by the interpretation algorithm. It is shown that the percentage of error is very small, ±2% in the radius estimation. For example; the radius bone with radii of 30mm produces ±0.48mm of dimensional error. The distribution of the percentage of error is hypothesised to be Gaussian with zero-mean, but the number of evaluated samples is too small to conclude this.

The results of the interpretation showed that the internal radius can be measured with greater consistency than the external radius. Uncertainty in measuring the external radius is an important factor in the risk estimation function. As a result of the interpretation, the maximum error of the external radius is less than 1.6% and less than 1.1% of the internal, which caused a 5% change of risk estimation function (see Appendix A.4).

With 99% confidence, the margin of error is less than 1% in the radius thickness (both internal and external). The margin of error in measuring the radius thickness in female

subjects showed a very narrow gap of 0.5% in 95% confidence. This is helps to indicate a high risk of fracture in female subjects with accuracy since female have the higher risk of fracture than male due to menopause (Pande *et al.* 2004).

There is evidence to show that model-based interpretation is effective as in each case a valid interpretation was produced and evaluated.

5.4 Evaluations of the risk of fracture

A logarithmic scale was used to estimate the risk of fracture estimation because the range of values was large. The data showed a bimodal distribution between subjects who had experienced a fracture and those who had not, which supported the Connectivity Index and Hole Area (Gordony 1998).

Using the mean of the risk of a fracture showed a promising result for differentiating those at a high risk of a fracture with a 0% of false negative and less than 5% false positive error rate. However, the risk estimate has a maximum error at 5% caused by an interpretation process. This implies that samples between ±5% of the estimation cannot be determined by this method because it is where false positives and false negatives can occur.

Student T-score showed that the risk estimations between fractured and non-fractured subjects are different with 92% confidence. This might be unacceptable for scientific determination which requires at least 95% confidence. However, this value may be closer to the standard 95% if more samples are to be tested.

6 CONCLUSIONS

We have shown an alternative technique to the BMD method for estimating the risk of a Colles' fracture. This technique used a plain radiograph of the forearm to assess the risk of fracture by measuring the internal and external radius of the radius bone, which were used in turn to estimate the stress on the bone. Model-based interpretation, in which a model consisted of 7 segments of X-ray attenuation profile across the radius bone, was used to estimate the internal and external radius.

An interpretation of unseen grey-level profile matching with the model showed to be reliable, contributing less than 1% of the margin of error (both internal and external radius estimates) with 99% confidence. The analysis of the risk of a bone fracture assessment indicates that the method developed has the potential to provide a reliable estimation of the risk of fracture. The error rates indicate that the uncertainty in estimation of the inner and outer radius of the bone was shown to have an impact on the accuracy of risk estimation increasing the error rates to almost 5%. The risk estimation of fractured and non-fracture subjects showed a bivariate distribution, confirmed by Student's t-test of 92% in population difference.

This project showed that it is possible to screen for an increased risk sample of a Colles' fracture using a development of the model-based interpretation of grey-level profiles across the radius bone from an ordinary X-ray image of the forearm.

A APPENDIX

A.1 Considerations of the position of measurement

A hollow cylinder is valid to model the radius bone if the inner and outer radius of the cylinder can be measured. Figure A 1.1 illustrated the radius bone regions where the bone profile can be taken as the following descriptions.

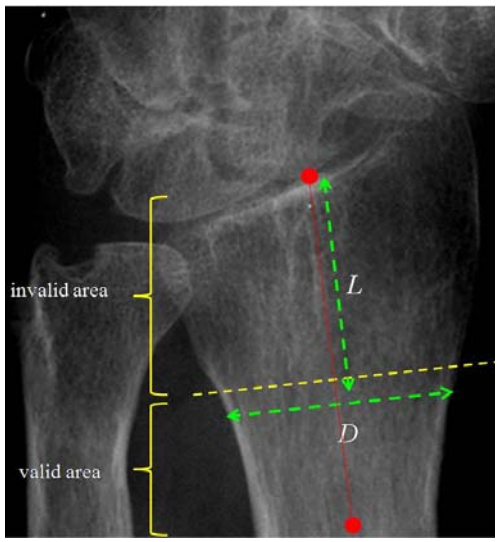

Figure A 1.1 Valid and invalid positions for measuring the thickness of cortical bone determined by the clarity of the contrast at the bone wall.

Invalid area — the area that bone contents are dense and the wall of cortical bone is not obviously noticed. The cortical thickness cannot be measured within this area as the shape is more complex in the vicinity of the joints. Consequently the cylindrical model of the radius would not be appropriate.

Valid area — the area that cylindrical model considered appropriate. The bone edge of this area is apparent and the radius width is not change rapidly. This area is suitable for measuring the bone thickness to determine the risk of fracture.

Valid position — the positions that the both side of the bone walls began to be parallel and the bone thickness is apparent as seen in Figure A 1.1 as a dash-line. This line can be determined without expert knowledge of wrist radiograph.

We evaluate the valid position by defining two parameters which were:

L	is	the length from the head of the radius bone to the profile, along the mid line of the bone
D	is	the width of the bone at the measured position.

A line was drawn along the axis of the radius and the diameter estimated at various points along this line. The point at which the rate of change of the diameter is small can be identified. 20 images (10 male and 10 female subjects) were measured the diameter at various distances from the head of the radius bone.

Figure A 1.2 showed the relationship between *L* and *D*, which fitted to the polynomial order 2 with R^2=0.9831, computed by least squares regression on vertical offsets.

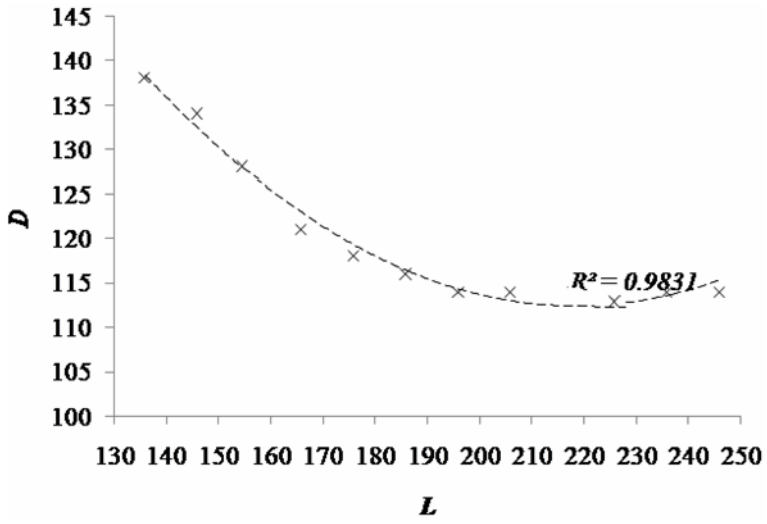

Figure A 1.2 Variation in diameter (*D)* with distance from the head (*L)* of the radius bone.

As shown in Figure A.13, a position that the measurement should be taken appear to be the position that radius thickness becomes unchanged (X_n). This can be done by determining the derivative function of the radius thickness (X_1...X_n)

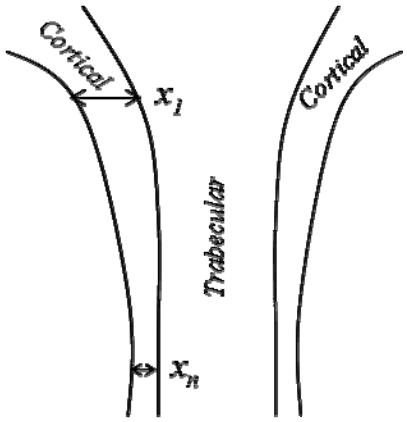

Figure A 1.3 The change of cortical bone thickness along the radius bone.

Time did not permit the method to standardise the measurement position to be evaluated. We assumed that radiographs used in this experiment are the representative of the entire groups because they were selected randomly with bone size difference. To ensure that profiles are always collected that locations beyond the valid position, we can simply use the maximum length as shown in Figure A 1.4.

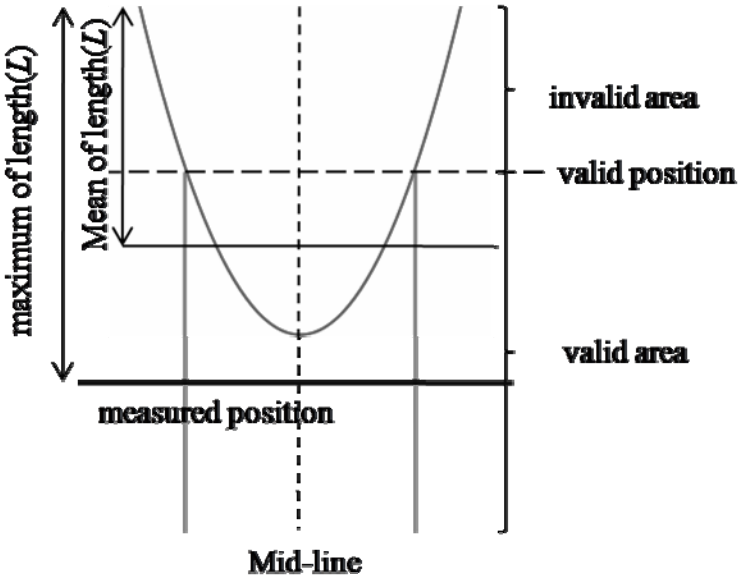

Figure A 1.4 Using maximum length as fixed length criteria to collect a profile within valid area

In this project we used the fixed-length criteria, which are thereby the maxima of L, to collect the bone profiles. The fixed-length criteria are:

$$L_{male} = 170 \text{ px } (25.5 \text{ mm}), L_{female} = 162 \text{ px } (24.4 \text{ mm})$$

The position of measurement from these fixed-length criteria may be not close to the optimal measured position but it can be guaranteed that the profile of this position is valid to measure the bone thickness.

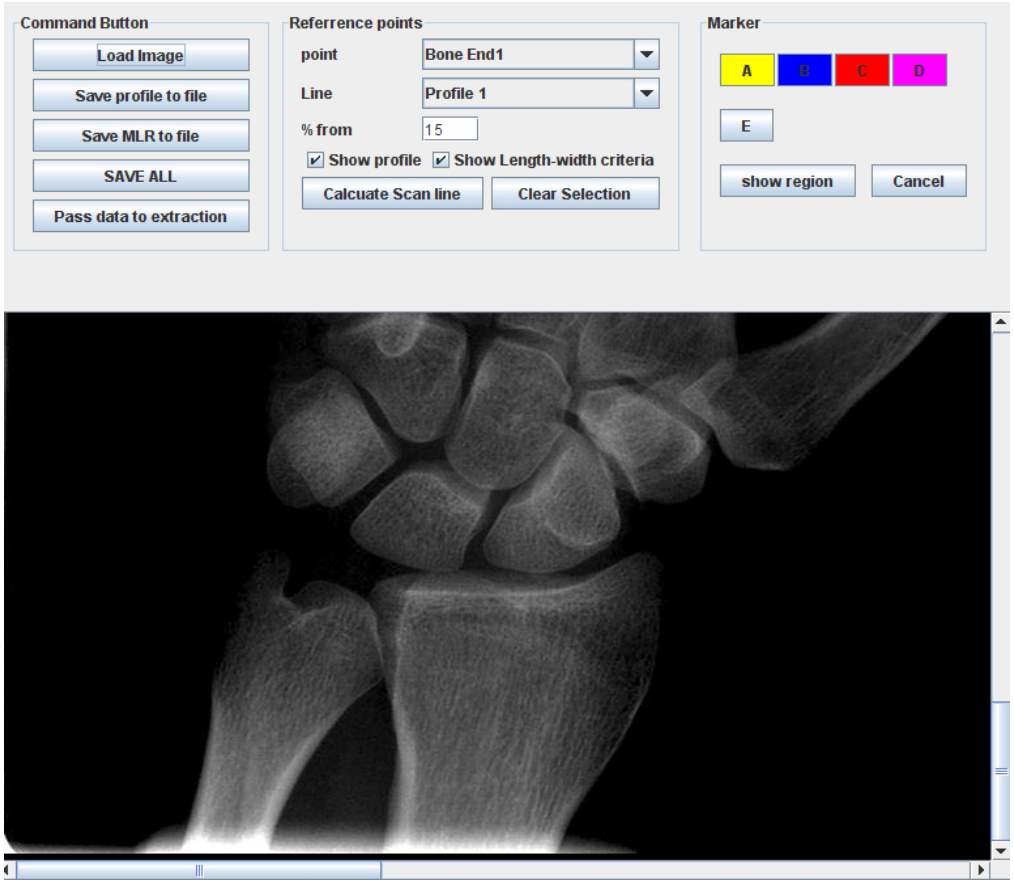

Figure A 1.5 User interface of profile collection program

Figure A 1.5 showed the user interface of the profile collection program. First of all, users need to load the radiographs from local files in JPG or PNG format into the program to extract the profiles. The profiles can be collected according to the scan lines which are located by the user. The line along in which the grey-level profile is to be sampled can be dragged to the desired position. The profiles and likelihood ratio are computed and are available in the profiles collection dialog.

The profile data and the likelihood ratios are saved as ASCII with suffixes of ".pro" and ".mlr", respectively. The position of the markers (A, B, C and D) can also be set, as shown in the Figure A 1.5 in order to create the region of interest of profile collection. Position E is the location in where the head of the radius bone was located.

A.2 Alternative bone profile model

This project proposed a 7-segment piece-wise model for the grey-level profile of the radius bone X-ray. The results of interpretation showed that measuring of the radius bone thinner and outer radius was subject to an uncertainty of less than 2%. The variability of the profile across the centre of the bone makes matching to this region problematic

In an alternative model of the grey-level pattern of an X-ray across the forearm the piece-wise linear model could be replaced by polynomial curves (P_1 and P_2) and a logarithmic curve (L_1) as shown in Figure A 2.1; this notion is inspired by Lee's study (Lee 2008).

Unfortunately, this project did not cover the other models of the bone profile as the time constrain. This model needs to be investigated if there is a basis that it can provide a better result of matching.

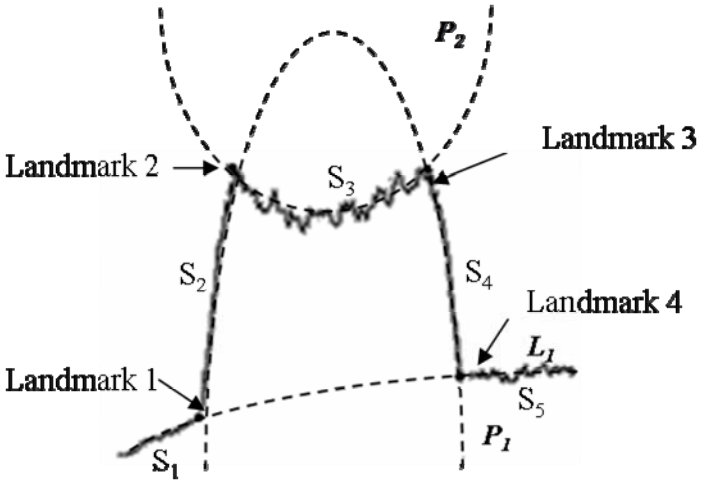

Figure A 2.1 An alternative model for the grey-level profile from an X-ray of the forearm, using a polynomial functions.

A.3 Risk fracture estimation and sensitivity analysis

Function for describing the risk of a fracture

$$\frac{4r_o}{\left(r_o^4 - r_i^4\right)}$$

$$\frac{4r_o}{\left(r_o - r_i\right)\left(r_o + r_i\right)\left(r_o^2 + r_i^2\right)}$$

Since $\Delta r = r_o - r_i$ and $r_o \sim r_i$, this can be reduced to:

$$\delta\left(r_o, \Delta r\right) = \frac{1}{r_o^2 \Delta r}$$

Let:

$$\delta(r_o, \Delta r) = f(r_o) g(r_o, r_i)$$

When

$$f(r_o) = \frac{1}{r_o^2}, g(r_o, r_i) = \frac{1}{(r_o - r_i)}$$

Then:

$$(fg)' = f'g + fg'$$

The derivative of the function for estimating the risk of a fracture is

$$\frac{\partial \delta}{\partial r_o} = \frac{\ln\left(\Delta r\right)}{r_o^2} + \frac{2}{\left(\Delta r\right)\left(r_o\right)}$$

The function for estimating the risk of a fracture is plotted in Figure A 3.1 and showed that the risk increases significantly when r_o and Δr are small. It also showed that the major parameter in the increasing of the risk factor is the external diameter of the bone, r_o.

The sensitivity analysis of the function for assessing the risk of fracture is plotted in Figure A.9, and showed that the variation in risk is small when Δr is low. Again the sensitivity of the risk estimation using this function is more critical with respect to the estimation of the external radius.

This interpretation of the function for estimating the risk of a fracture gives reason to believe that the estimation of the external radius is the most critical parameter.

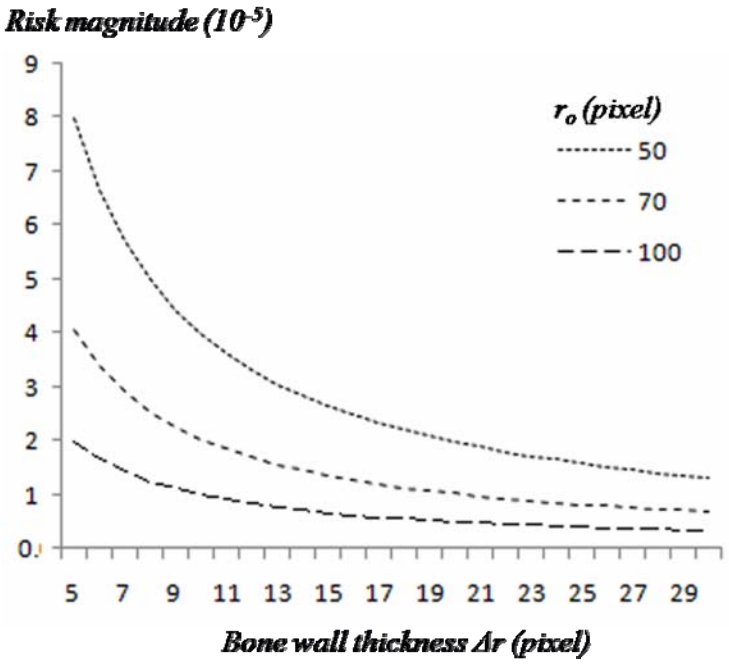

Figure A 3.1 Plot of fracture risk function.

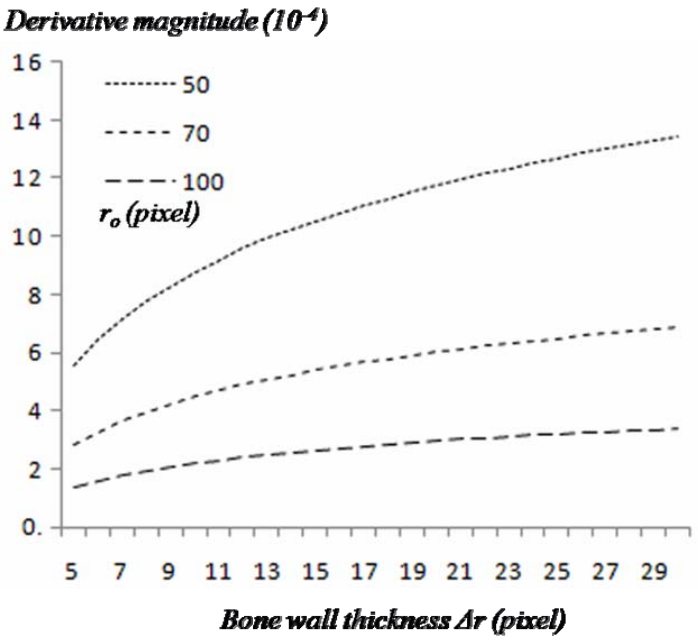

Figure A 3.2 Plot of derivative of the fracture risk function.

A.4 Maximum error of risk estimation

Let the risk estimation function is

$$\delta(r_o, \Delta r) = \frac{1}{r_o^2 \Delta r}$$

As a result of interpretation program, the maximum error of r_o is less than 1.6% and the maximum error of r_i is less than 1.1%.

Let substitute parameters with $1.016r_o$ and $1.011r_i$ to find the maximum error of the risk estimation function using upper bound as the following expression

$$\frac{1}{(1.016r_o)^2\left[(1.016r_o - 1.011r_i)\right]}$$

Which equal to lower bound of

$$\left\lfloor \frac{1}{(1.032)r_o^{\,2}(1.027)\Delta r} \right\rfloor$$

Let substitute risk estimation function with $\delta(r_o, \Delta r)$

$$0.9503\ \delta(r_o, \Delta r)$$

Therefore, the expression showed that with 1.6% external radius error and 1.1% internal error from the interpretation process caused at most 4.97% of risk estimation.

A.5 UML design of software interpretation

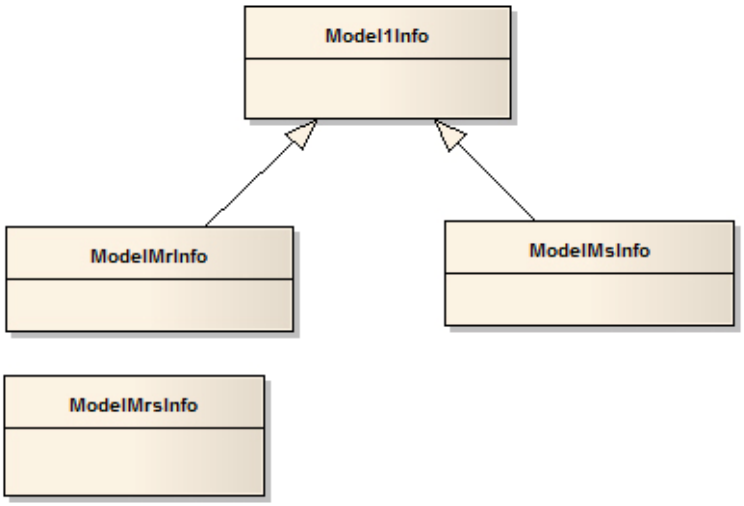

Figure A 5.1 Class diagram of model package

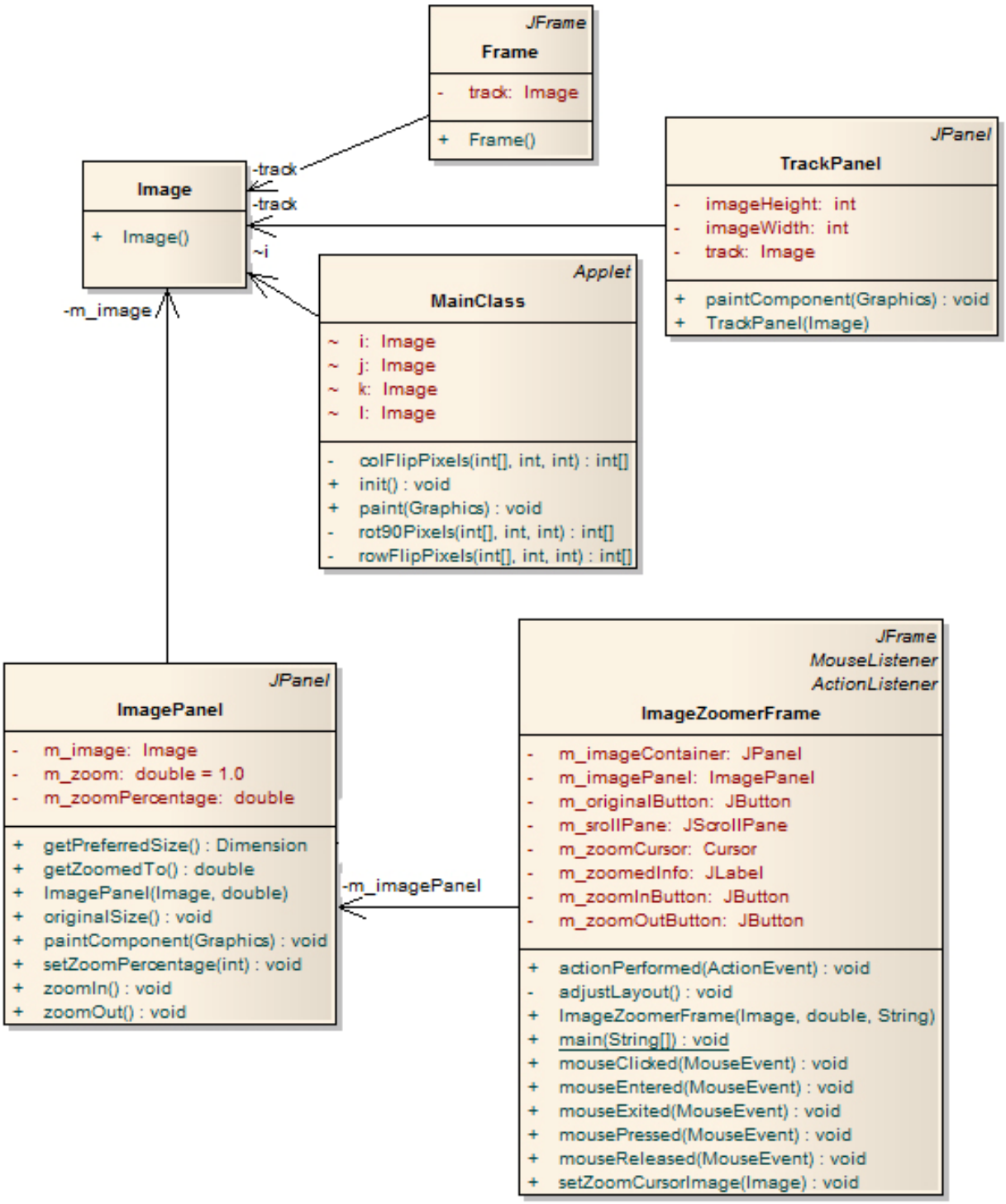

Figure A 5.2 Class diagram of collection package

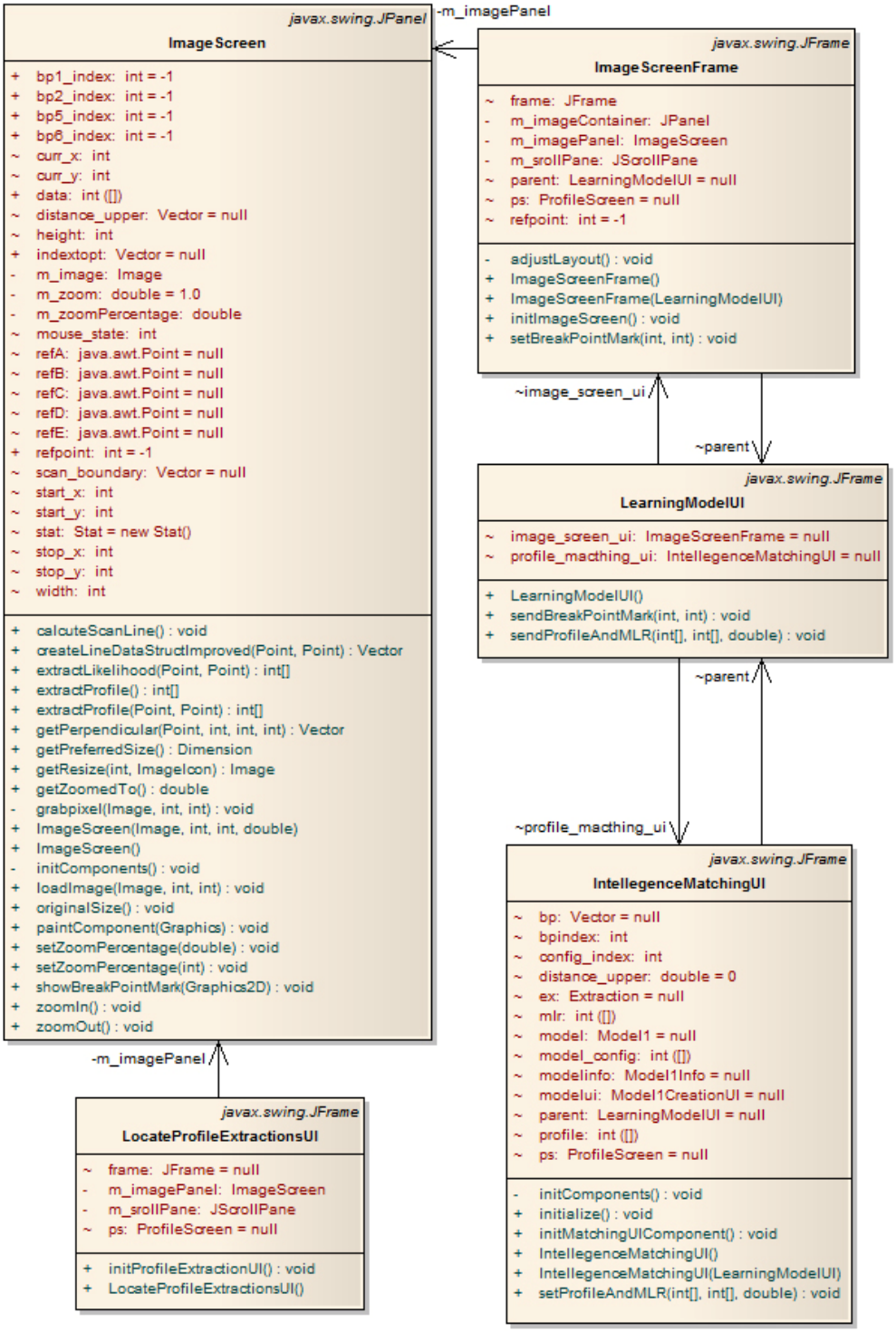

Figure A 5.3 Class diagram of main program

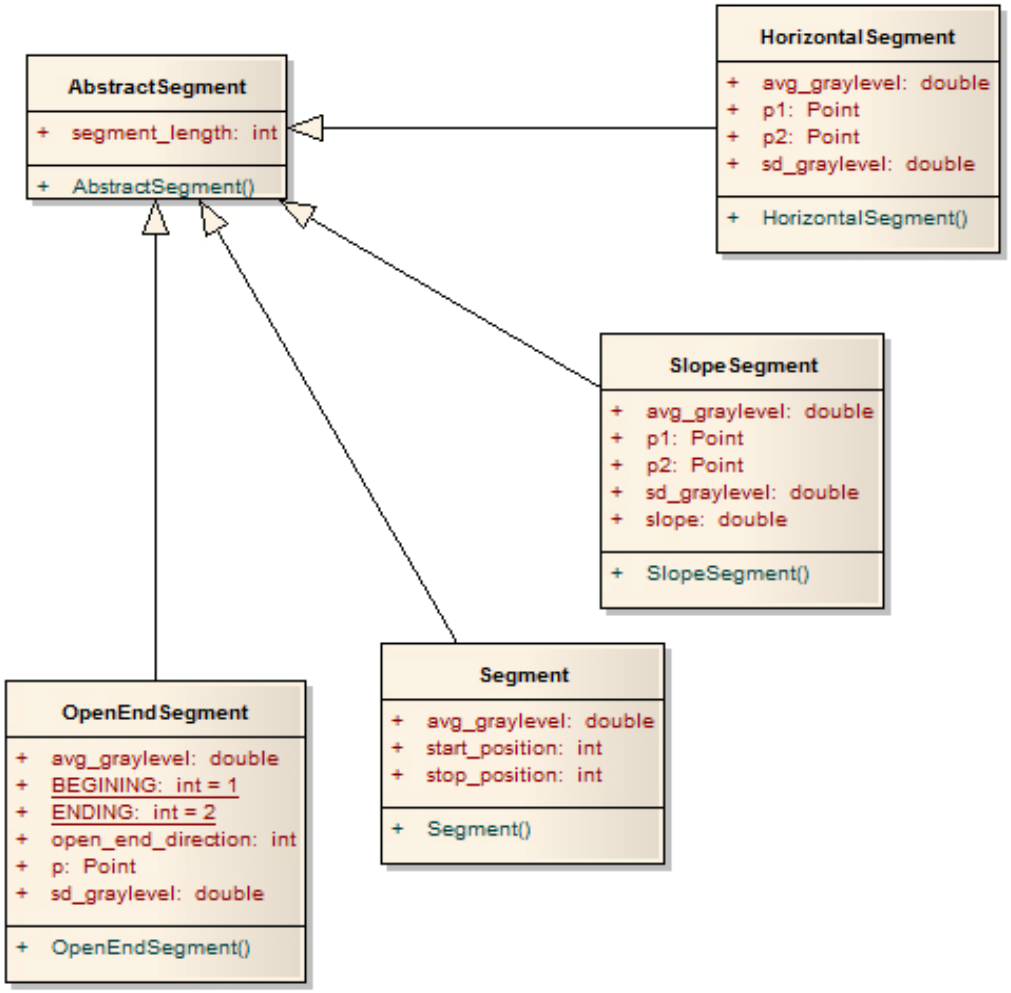

Figure A 5.4 Class diagram of utility package (1)

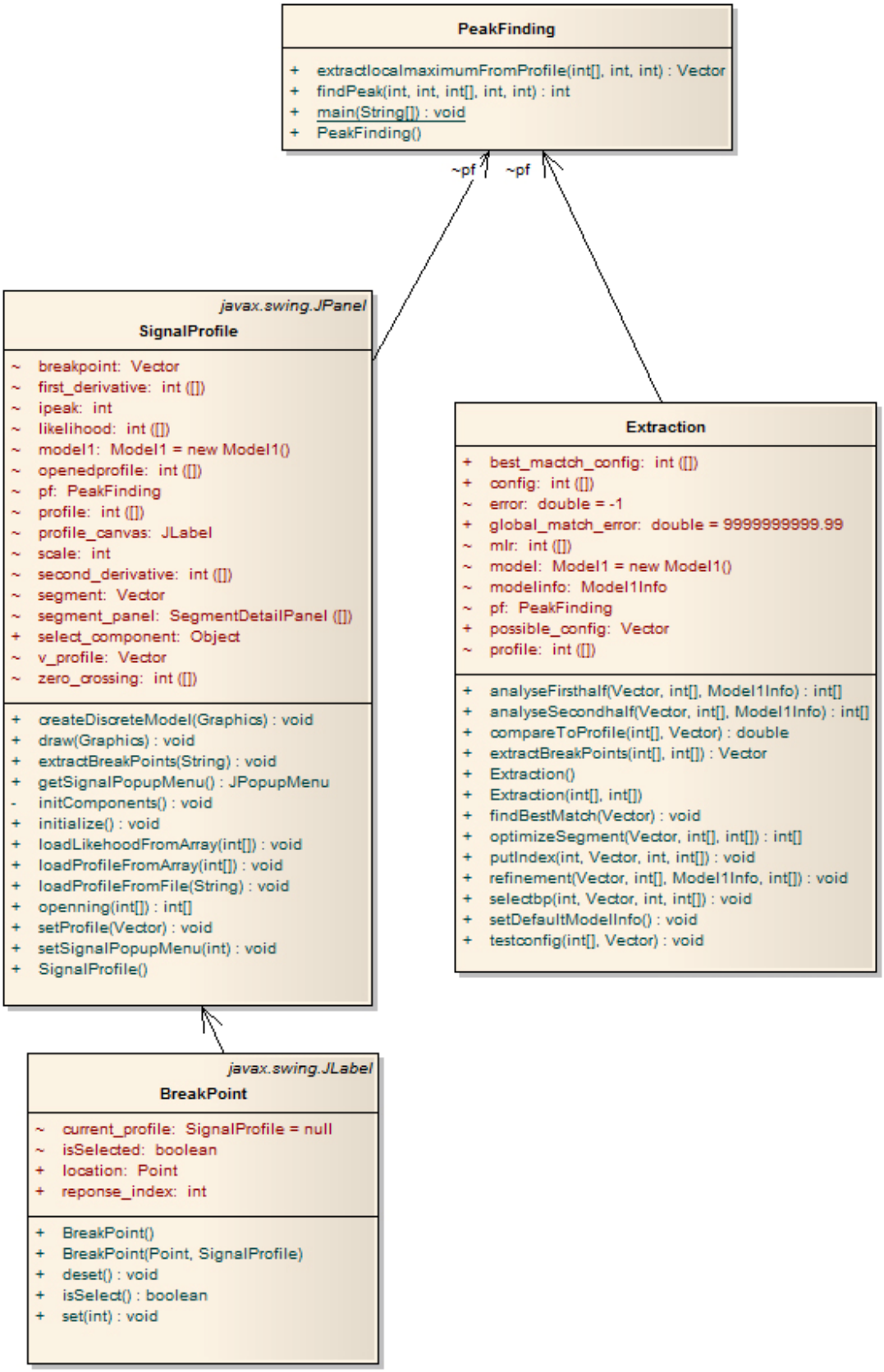

Figure A 5.5 Class diagram of utility package (2)

REFERENCES

C. J. Taylor, A. Lanitis, G. Edwards, P. Smyth and A. C. W. Kothcheff (1997). “Model-based interpretation of complex and variable images”, Philosophical Transactions: Biological Sciences. **352**: 1267-1274

C. L. Gordony, J. D. Adachiz and N. Christoforou (1996). "In vivo assessment of trabecular bone structure at the distal radius from high-resolution computed tomography images." Phys. Med. Biol. **41**: 495–508.

D. Pycock, A. J. Goode, S. A. Harman (2001). "Robust model-based signal analysis and identification." Pattern Recognition **34**: 2181-2199.

G. Behiels, P. Suetens (2000). “Statistical Shape Model-based Segmentation of digital X-ray Images.” Medical Image Computing and Computer-Assisted Intervention. **2208**: 301-308

B. C. Hopson (2000, September, 2007). "Fractures, Wrist: Treatment & Medication." Retrieved March, 2009, from http://emedicine.medscape.com/article/828746-treatment.

C. Hoynak (2000). "Broken Wrist AKA: Colles Fracture." Retrieved September, 2008, from http://www.physioroom.com/injuries/hand_and_wrist/colles_fracture_full.php.

J. Xue (2002). "Buckling of a non-uniform, long cylindrical shell subjected to external hydrostatic pressure." Engineering Structures **24**: 1027-1034.

M. Muller , P. Moilanen , V. Bousson , M. Talmant , P. Laugier (2008). "Prediction of bone mechanical properties using QUS and pQCT: Study of the human distal radius.", Medical Engineering & Physics **30**: 761–767.

D. Nelson (2005, January 2, 2009). "a Distal Radius Fracture." Retrieved January 12, 2009, from http://www.davidlnelson.md/Wrist_Fracture.htm.

K. C. Pande (2004). "Digital X-ray radiogrammerry." Indian Journal of orthopadics **38**(2): 73-79.

P. Saparina, J. Kurths, G. Beller, W. Gowin (2006). "Segmentation of bone CT images and assessment of bone structure using measures of complexity." Med. Phys. **33**(10): 3857-3873.

Z. Peter, V. Bousson, et al. (2008). "A constrained region growing approach based on watershed for the segmentation of low contrast structures in bone micro-CT images." Pattern Recognition **41**(7): 2358-2368.

D. M. Preston (2007, December 21, 2007). "Wrist Fractures." Retrieved December, 2008, from http://www.patient.co.uk/showdoc/40001429/.

D. Roylance (2000). “Statics of Bending: Shear and Bending Moment Diagrams”. Cambridge, Massachusetts Institute of Technology.

S. Lee, J. W. Lee, D. S. Yoo, and S. Kim (2007). Bone Mineral Density Estimation using the Filling Factor of the Radius X-ray Image. Proceedings of the 29th Annual International Conference of the IEEE EMBS :5533-5.

T. F. Cootes, H. Cooper, and J. Graha (1995). "Active Shape Models-Their Training and Application." COMPUTER VISION AND IMAGE UNDERSTANDING **61**(1): 38-59.

C. J. Taylor (1988). “Boundary Cue Operators for Model Based Image Processing”, Wolfson Image Analysis Unit, Department of Medical Biophysics, University of Manchester.

T. J. Hutton (2000). "An evaluation of active shape models for the automatic identification of cephalometric landmarks." European Journal of Orthodontics **22**: 499-508.

V. Chalana, Y. K. (1997). "A Methodology for Evaluation of Boundary Detection Algorithms on Medical Images." IEEE TRANSACTIONS ON MEDICAL IMAGING, **16**(5): 642 -652.

W. Yue, D. Yin, et al. (2006). "Automated 2-D Cephalometric Analysis on X-ray Images by a Model-Based Approach." Biomedical Engineering, IEEE Transactions on **53**(8): 1615-1623.